2018

Heterostructures for Electrochemical Hydrogen Evolution Reaction: A Review

Guoqiang Zhao
University of Wollongong, gz815@uowmail.edu.au

Kun Rui
University of Wollongong, krui@uow.edu.au

Shi Xue Dou
University of Wollongong, shi@uow.edu.au

Wenping Sun
University of Wollongong, wenping@uow.edu.au

Publication Details

Zhao, G., Rui, K., Dou, S. Xue. & Sun, W. (2018). Heterostructures for Electrochemical Hydrogen Evolution Reaction: A Review. Advanced Functional Materials, 28 (43), 1803291-1-1803291-26.

Heterostructures for Electrochemical Hydrogen Evolution Reaction: A Review

Abstract

Developing sustainable and renewable energy sources along with efficient energy storage and conversion technologies is vital to address environmental and energy challenges. Electrochemical water splitting coupling with grid-scale renewable energy harvesting technologies is becoming one of the most promising approaches. Besides, hydrogen with the highest mass-energy density of any fuel is regarded as the ultimate clean energy carrier. The realization of practical water splitting depends heavily on the development of low-cost, highly active, and durable catalysts for hydrogen evolution reactions (HERs) and oxygen evolution reactions (OERs). Recently, heterostructured catalysts, which are generally composed of electrochemical active materials and various functional additives, have demonstrated extraordinary electrocatalytic performance toward HER and OER, and particularly a number of precious-metal-free heterostructures delivered comparable activity with precious-metal-based catalysts. Herein, an overview is presented of recent research progress on heterostructured HER catalysts. It starts with summarizing the fundamentals of HER and approaches for evaluating HER activity. Then, the design and synthesis of heterostructures, electrochemical performance, and the related mechanisms for performance enhancement are discussed. Finally, the future opportunities and challenges are highlighted for the development of heterostructured HER catalysts from the points of view of both fundamental understandings and practical applications.

Disciplines

Engineering | Physical Sciences and Mathematics

Publication Details

Zhao, G., Rui, K., Dou, S. Xue. & Sun, W. (2018). Heterostructures for Electrochemical Hydrogen Evolution Reaction: A Review. Advanced Functional Materials, 28 (43), 1803291-1-1803291-26.

WILEY-VCH

DOI: 10.1002/ ((please add manuscript number))
Article type: Review

Heterostructures for Electrochemical Hydrogen Evolution Reaction: A Review

*Guoqiang Zhao, Kun Rui, Shi Xue Dou, Wenping Sun**

G. Q. Zhao, Dr. K. Rui, Prof. S. X. Dou, Dr. W. P. Sun
Institute for Superconducting and Electronic Materials, Australian Institute of Innovative Materials, University of Wollongong, Wollongong, NSW 2522, Australia
E-mail: wenping@uow.edu.au

Keywords: heterostructures, hydrogen evolution reaction, mechanism, water splitting, electrocatalysis

Abstract:

Developing sustainable and renewable energy sources along with efficient energy storage and conversion technologies is vital to address the environmental and energy challenges. Electrochemical water splitting coupling with grid-scale renewable energy harvesting technologies is becoming one of the most promising approaches. Besides, hydrogen with the highest mass-energy density of any fuel is regarded as the ultimate clean energy carrier. The realization of practical water splitting depends heavily on the development of low-cost, highly active, and durable catalysts for hydrogen evolution reaction (HER) and oxygen evolution reaction (OER). Recently, heterostructured catalysts, which are generally composed of electrochemical active materials and various functional additives, have demonstrated extraordinary electrocatalytic performance toward HER and OER, and particularly a number of precious metal-free heterostructures delivered comparable activity with precious metal-based catalysts. In this review, we present an overview of recent research progress on heterostructured HER catalysts. We start with summarizing the fundamentals of HER and approaches for evaluating HER activity. Then, the design and synthesis of heterostructures,

electrochemical performance, and the related mechanisms for performance enhancement are discussed. Finally, we highlight the future opportunities and challenges for the development of heterostructured HER catalysts from the points of view of both fundamental understandings and practical applications.

1. Introduction

Environmental pollution, global warming, and energy crisis caused by massive fossil fuel combustion have been the focus of world attention.[1] According to a report from the International Energy Agency, the global energy demand will expand by 30% by 2040, and the CO_2 emissions will reach as large as 35.7 Gt per year in 2040.[2] Therefore, establishing a global-scale clean and sustainable energy system is on the top challenges facing the humanity. To this end, countries from all over the world are taking steps to stimulating the development and application of renewable energies such as hydropower, solar, and wind energy, etc.[3-4] However, the spatial and temporal discontinuities of these renewable energy resources result in low energy delivery efficiency. In addition to developing low-cost grid-scale energy storage systems, another promising solution is to convert these renewable energies into chemical fuels that can be easily stored and transported. Hydrogen (H_2), with the highest gravimetric energy density among all chemical fuels (142 MJ Kg^{-1}, upper heating value),[5] is considered as the ultimate clean energy carrier, which would significantly mitigate the environmental concerns due to zero emission of carbonaceous species.

Photoelectrochemical and electrochemical water splitting are two possible strategies to realizing solar-to-hydrogen conversion. However, due to the limitation of the working current densities,[6] photoelectrochemical water splitting devices require much larger electrode area

than electrochemical water splitting systems to generate the same amount of gas per unit time, resulting in restrictions in choosing viable catalysts and suitable construction locations.[7-8] Moreover, other renewable energies are naturally excluded from the photoelectrochemical avenue. Therefore, despite of lower solar-to-hydrogen efficiency than the direct photoelectrochemical route, the electrochemical water splitting is more attractive due to the higher flexibility and applicability. Combining grid-scale renewable energy harvesting infrastructures with electrochemical water splitting devices can efficiently convert the intermittent electricity obtained from renewable energies into more valuable H_2 and thereby enhance the diversity of renewable energy utilization.[9] **Figure 1** shows a sustainable pathway for the circulation of hydrogen energy regarding the combination of renewable energy harvesting and electrochemical water splitting. This hydrogen production process is CO_2-free and requires only water and electricity, [10-11] in sharp contrast to the steam reforming reaction which is the primary hydrogen production approach in the industry and involves fossil fuels consumption and CO_2 emission.[12-13] Besides, the electrochemical water splitting produces H_2 with a high purity that can directly be used as either an industrial feedstock or the fuel gas for householding. Furthermore, H_2 is the ideal fuel for proton-exchange membrane fuel cells (PEMFCs), which is a high efficient energy conversion device and is also a promising candidate for electric vehicle power systems. Therefore, it is pivotal to develop efficient water electrolysis systems and thus enable the non-polluting H_2 production for establishing the clean and sustainable energy system for the future.

In a typical water electrolysis system, H_2 and O_2 is produced at the cathode and the anode through the hydrogen evolution reaction (HER) and oxygen evolution reaction (OER),

respectively, and an external current is applied to overcome the energy barrier of the reaction (237 kJ mol^{-1}). Although the water electrolysis theory is straightforward, the large-scale application of water splitting for H_2 production is still absent in reality today.[14] The first commercial demonstration of water electrolysis dates back to as early as the 1890s. However, after more than 100 years of development, electrochemical water splitting contributes only 4% of H_2 supply worldwide,[15] which is in great part due to the high cost and low efficiency. In practice, the energy conversion efficiency of a commercial electrolyzer system is about 56–73%.[16] To address this issue, we must choose proper catalysts to improve the energy conversion efficiency. At present, noble-metal-based catalysts remain to be the most efficient catalysts for HER and OER, and Pt is the state-of-the-art catalyst for HER.[17-20] Therefore, developing earth-abundant catalysts with high activity becomes one of the top priorities for the development of economic and efficient water electrolysis systems. To date, various earth-abundant catalysts with considerable catalytic activity towards OER and in particular HER have been reported.[21-28] With regard to HER, transition metal dichalcogenides (TMDs),[29-34] transition metal phosphides (TMPs),[35-38] carbides,[39-41] and nitrides,[42-43] are extensively investigated. Recently, a variety of heterostructured catalysts stand out from the crowd, showing extraordinary catalytic performance towards electrochemical water splitting over their counterparts.[44-48] For example, Gao et al. reported a $MoS_2/CoSe_2$ heterostructure catalyst by depositing MoS_2 on the surface of $CoSe_2$. The $MoS_2/CoSe_2$ heterostructure exhibited excellent HER performance in 0.5 M H_2SO_4 with an overpotential of 68 mV at 10 mA cm^{-2}, a Tafel slope of 36 mV dec^{-1}, and good performance durability.[49] Chen et al. synthesized a three-dimensional (3D) core/shell catalyst composed of metallic Co cores and

amorphous Co_3O_4 shells, and the Co/Co_3O_4 heterostructure delivered 10 mA cm^{-2} at a low overpotential of merely 90 mV in 1 M KOH.[50]

The concept of heterostructure originates from semiconductor physics. According to the definition, heterostructures consist of abundant heterojunctions—the interfaces between different components, and heterostructures are semiconductor structures where the chemical composition changes with position.[51] With the intercrossing and merging of knowledge network, the concept of heterostructure has gone beyond semiconductor physics. More generally, heterostructures may be defined as the composite structures that consist of interfaces formed by different solid-state materials, including conductors, insulators as well as semiconductors. The concept of heterostructure hereinafter in this review refers to this generalized definition. Accordingly, a heterostructured catalyst consists of two or more types of materials that are usually physically or chemically bonded together. From the perspective of the HER catalytic activity of the catalysts, the components in a heterostructure could be either active or non-active. Nevertheless, most heterostructured catalysts, including active/active and active/non-active types of heterostructures, exhibit higher HER activities than the single counterpart due to a variety of advantages that the heterostructured catalysts might possess, as illustrated in **Figure 2.** Firstly, constructing heterostructured HER catalysts is an efficient approach to increasing the number of active sites. Most of these heterostructured HER catalysts possess refined nanostructures with substantially exposed edges, which provide sufficient adsorption sites for the intermediates of HER.[52-54] Secondly, in addition to further increasing the number of active sites and enhancing electrical conductivity, introducing macroscopic substrates such as nickel foam (NF), carbon cloth (CC)

into heterostructures can enable fast mass diffusion, which is vital to reducing overpotential at high current densities.[55-57] Thirdly, the performance durability of the catalysts can be improved by constructing some well-defined nanostructures.[53] Taking a core-shell structure as an example, the active but unstable species can be protected by a thin layer of stable species, which enables a long-life HER activity. Fourthly, the difference between the electronegativity of the different components in the heterostructured catalysts may induce electron transfer between different components, which usually can be revealed by the binding energy shift in XPS spectra. The electron redistribution will regulate the electronic structures or the band structures of the components, which is critical to the superior HER activity of some heterostructures.[43, 58-59] Finally, the so-called synergistic effect also contributes significantly to the enhanced HER kinetics of the heterostructures.[49, 60] Heterostructured catalysts are designed with specific attention on introducing additional water adsorption/dissociation sites for alkaline HER, and transition metal hydroxides/oxides are most extensively explored as water adsorption/dissociation promoters.[61-63]

Although a variety of heterostructured catalysts exhibit decent HER activity over a wide pH range and/or show multifunctional activity for both HER and OER, they are not included in this review. Considering that conventional water electrolysis facilities generally work at either very high or very low pH,[8] this review focuses on the recent development of the heterostructured catalysts that work in either acidic or alkaline solutions, and a brief summary of these heterostructures is presented in **Table 1** and **Table 2**. In this review, we mainly summarize the catalyst design and synthesis methodologies, and discuss the related mechanisms. We start with briefly reviewing the HER reaction mechanism and the general

approaches for evaluating catalytic performance. Then, we introduce the state-of-the-art heterostructured HER catalysts, with emphasis on the design and synthesis strategies as well as the mechanisms for the enhanced catalytic activity. Finally, we highlight the opportunities and challenges of the heterostructured catalysts and provide perspectives for the future research.

2. Mechanisms of electrochemical HER

Electrocatalytic HER is essentially an electrochemical process where redox reactions take place at the electrode/electrolyte interface. Depending on the pH value of the electrolyte, H_2 is generated via the reduction of either proton (H^+) or H_2O, both of which involve a series of elementary steps.

2.1 HER in acidic media

It has generally been accepted that the HER at the surface of various catalysts involves two successive steps in acidic media.[64-66] At the beginning of HER, a H^+ adsorbs on the catalyst surface to form an adsorbed hydrogen atom (H*), where * represents an active site on the catalyst surface. This process is called the Volmer step or the discharge step (equation 1). Then a H* combines with a H^+ and an electron (e^-) to form a H_2 molecule, as described in equation 2, which is named as the Heyrovsky step or the electrochemical desorption step. Alternatively, H_2 could be formed via the Tafel step which is also known as the chemical desorption step, i.e. the combination of two H* on the catalyst surface (equation 3). The overall reaction of HER is represented in equation 4, the standard electrode potential (E°) of which is used as the reference for evaluating the standard electrode potential of electrochemical reactions.[67]

$$H^+ + e^- \rightarrow H^* \quad (1)$$

$$H^* + H^+ + e^- \rightarrow H_2 \quad (2)$$

$$2H^* \rightarrow H_2 \quad (3)$$

$$2H^+ + 2e^- \rightarrow H_2 \quad (4)$$

According to the Sabatier principle,[68] the HER kinetics strongly hinges on the interaction between the catalyst and H*.[69] By plotting the reaction rate of the HER on various catalyst surface vs. the hydride formation energy, S. Trasatti constructed the first volcano curve for the HER.[70] The hydride formation energy was used to describe the adsorption behavior due to the unavailability of neither experimental nor theoretical data for the hydrogen adsorption energy ($\Delta G°_H$) at that time. In 2004, Nørskov's group collected experimental data of exchange current densities for HER on various metals, calculated the corresponding adsorption energies using the density functional theory (DFT), and presented the first modern volcano plots.[71] The results perfectly elucidate the origin of the superior HER activity of Pt and provide an intuitive description for the dependence of HER activity on hydrogen binding energy. As a successful paradigm, the edge sites of MoS_2 were predicted to possess high HER activity based on a close-to-neutral $\Delta G°_H$ of MoS_2 edges,[72] which afterwards were confirmed by experiments.[73] Since then, attempts to expose more edges of MoS_2 have achieved dramatic success in developing advanced HER catalysts,[74-75] which highlights the importance of combining theories and the practice in developing advanced HER catalysts. Thanks to DFT calculations which is an integral part of the modern catalysis science, $\Delta G°_H$ now can straightforward be obtained and has played an indispensable role in interpreting the intrinsic electrocatalytic activity of HER catalysts.[76]

2.2 HER in alkaline media

As for the HER in alkaline media, $\Delta G°_H$ still works for describing the adsorption behavior of hydrogen on the surface of catalysts. It is interesting to note that the volcano plot in alkaline media shift only up and down rather than left or right comparing with that in acidic solution.[77] Specifically, the exchange current densities of HER on most metal catalysts in alkaline solutions are two to three orders of magnitude smaller than in acidic electrolytes.[62, 78] One of the most important reasons for this inferior catalytic activity is that the alkaline HER proceeds via a distinct pathway from that in acidic solutions. Due to the lack of H^+, the HER in alkaline media starts from dissociating H_2O molecules to provide protons, which process is involved in both the Volmer step (equation 5 and the Heyrovsky step (equation 6) of alkaline HER, while the Tafel step remains the same with that in acid solutions. The overall reaction process is described in equation 7, and the E^o of this reaction vs. the standard hydrogen electrode (SHE) is -0.826 V.

$$H_2O + e^- \rightarrow H^* + OH^- \quad (5)$$

$$H^* + H_2O + e^- \rightarrow OH^- + H_2 \quad (6)$$

$$2H_2O + 2e^- \rightarrow 2OH^- + H_2 \quad (7)$$

As additional energy is required to generate protons in alkaline media, the HER kinetics on most catalysts is more sluggish in alkaline electrolytes. It has been reported that alkaline HER activity is controlled by a delicate balance between $\Delta G°_H$ and the energy required to dissociate H_2O.[66] However, a variety of HER catalysts including MoS_2, Co_2P are not favored for water dissociation process.[79-80] Consequently, promoting the water dissociation process while remaining a moderate hydrogen adsorption energy is a useful strategy to design

efficient catalysts toward alkaline HER.

3. General approaches for evaluating catalytic performance

3.1 Overpotential

Overpotential, the difference between the experimentally observed potential and the thermodynamically determined potential of an electrochemical reaction,[65] is regarded as one of the most important values for evaluating a water splitting catalyst since it is the large overpotential that results in the low energy conversion efficiency of the electrochemical water electrolysis system.[65] Linear sweep voltammetry (LSV) is commonly performed to obtain the overpotential, and small sweep rates (e.g., 2 mV s^{-1}, 5 mV s^{-1}) are usually employed to minimize the non-faradic current. The origin of the overpotential could be the activation of the reaction, the diffusion of charge carriers and the series resistance. To be more precise, the activation overpotential directly relates to the catalytic activity, whereas the overpotentials caused by the series resistance and diffusion of charge-carriers mostly stem from the water electrolysis system. Thus, the activation overpotential should be precisely evaluated to better assess the materials catalytic activity. Using a rotate disk electrode (RDE) system, where the electrode continuously rotates when recording linear sweep voltammetry (LSV) curves, can efficiently minimize the diffusion overpotential. Meanwhile, the resistance overpotential can be corrected by *IR* compensation (Equation 8), where I is the current flowing in the circuit and R_s is the series resistance.

$$E_{corrected} = E_{uncorrected} - IR_s \quad (8)$$

Conventionally, the overpotential at a current density of 10 mA cm^{-2}, corresponding to the working current density of the most cost-competitive photoelectrochemical water splitting

system, is introduced as a benchmark for evaluating catalyst performance.[81-82] The current density is usually determined with respect to the geometric area of the electrode, which can also be calculated based on the specific geometric area of the catalyst, the electrochemical active specific area (ECSA) of the catalyst, or the catalyst mass.

3.2 Tafel slope and exchange current density

Tafel slope is the slope of the linear region of a Tafel plot (overpotential vs. log |current density|), which can be obtained by replotting the corresponding LSV curve. Notably, Tafel slope can provide insights into the reaction mechanism of HER on the catalyst surface. The theoretical Tafel slope for the Volmer step, the Heyrovsky step and the Tafel step in HER is 120, 40 and 30 mV dec^{-1}, respectively.[64, 83] For example, the HER on the surface of the commercial Pt in 0.5 M H_2SO_4 is close to 30 mV dec^{-1}, indicating that the reaction proceeds via the Volmer-Tafel process and the rate-determining step (RDS) for the reaction is the Tafel step.[74] Generally, an extreme coverage of H* ($\theta \approx 0$ or ≈ 1) is assumed when using the Tafel slope to evaluate the RDS of HER. However, the Tafel slope is coverage-dependent in practice. Over-simplified interpretation of Tafel slope will lead to an inaccurate description of the reaction.[84]

The exchange current density of a reaction is the current density at the equilibrium potential where the cathodic current equals the anodic current.[65] It can be read out from the intersection of the extrapolated linear part of Tafel plots and the X-axis. Essentially, exchange current density reflects the intrinsic activity of charge transfer between electrode and electrolyte, and to catalyze a reaction is to promote the exchange current density.[85] The exchange current density tends to be larger on the surface of catalysts with higher catalytic

activity. For instance, the current density of HER on the surface of Pt, Ti, and Hg in 0.5 M H_2SO_4 is about 1, 10^{-5}, 10^{-9} mA cm^{-2}, respectively, representing the variations in their intrinsic activity.[86]

3.3 Turnover frequency

The turnover frequency (TOF) is the number of the product molecule generated per active site in unit time (equation 10).[87-88] According to the definition, H_2 should be collected to evaluate the number of the H_2 molecules. Assuming the Faradic efficiency of 100%, the theoretical number of H_2 can be calculated from the charge flowing through the circuit based on the Faraday's laws of electrolysis (equation 11), where n is the amount of substance (mol), I is current (A), z is electron number transferred per molecule, and F is the Faraday constant (96485 C mol^{-1}). Then a TOF vs. overpotential curve can be achieved (equation 12) according to equation 10 together with Equation 11. Consequently, calculating TOF largely hinge on determining the number of active sites, which can be evaluated by various methods including the copper underpotential deposition method,[29] calculating the number of molecules on the exposed surface,[89-91] or quantifying from CV tests,[92-94]. Apparently, to achieve a reasonable TOF or TOF-overpotential curve depends on how to define and evaluate the number of active sites. It is noteworthy that the overpotential value should always be indicated when reporting the TOF values since TOF increases with increasing overpotentials.

$$TOF = \frac{molecule\ number\ of\ \ product}{number\ of\ \ active\ sites} \times \frac{1}{unit\ time} \tag{10}$$

$$n = \frac{It}{zF} \tag{11}$$

$$TOF = \frac{I \times N_A}{zF \times number\ of\ \ active\ sites} \tag{12}$$

3.4 Stability

Stability, or durability, is an important descriptor of a catalyst in view of practical application, demonstrating the ability to maintain the original activity of a catalyst over a long range of time. The stability can be evaluated by recording the variation of the overpotential at a certain current density or recording the change of cathodic current density at an applied overpotential, over a period of time. It can also be evaluated by continuous cyclic voltammetry (CV) cycling. As LSV curves are usually recorded before and after the stability test, there will be an evident increase in the overpotential if the catalyst loses its activity quickly. It should be mentioned that the present approaches are focused on evaluating the stability under working conditions, and there lacks of effective approaches for stability evaluation under idle conditions.

4. Heterostructured catalysts for HER

Growing nanostructured catalysts on supportive substrates is one of the most effective approaches to alleviating the agglomeration of the active materials. The most commonly used substrates include NF, CC, titanium mesh (TM), carbon nanotubes (CNTs), graphene-based materials, 2D TMDs, and graphitic carbon nitride (g-CN), and so forth. These substrates can be divided into two categories: macroscopic substrates (e.g., CC, NF, TM) and nanostructured substrates (e.g., CNTs, graphene, TMDs, g-CN). The macroscopic substrates possess 3D reticular structures which can efficiently maximize the exposure of active sites, and these substrates can also act as good current collectors during electrochemical testing. However, it is not easy to evaluate the intrinsic activity of the catalysts since neither the mass loading nor the geometric area of active materials can be precisely determined. In this review, we will

mostly focus on the progress of nanostructured substrate-supported heterostructures and will not discuss those macroscopic substrate-supported heterostructures. Considering the difference of the HER mechanisms, we discuss the heterostructured catalysts in acidic and alkaline solutions separately.

4.1 Heterostructured catalysts for HER in acidic media

4.1.1 Carbonaceous material-supported heterostructures

In 2005, the MoS_2 (100) edges were found to bear a resemblance close to the active sites of hydrogenase enzymes, possessing a $\Delta G°_H$ of 0.08 eV at 50% hydrogen coverage.[72] Therefore, exposing more edge sites of MoS_2 has been recognized as a valid strategy toward increasing the HER catalytic activity of MoS_2.[95] In 2011, Li et al. prepared a MoS_2/RGO hybrid catalyst with MoS_2 nanoparticles grown on RGO nanosheets.[74] As revealed by the scanning electron microscopy (SEM) image (**Figure 3**a) and the transmission electron microscopy (TEM) image (inset in Figure 3a), nano-sized MoS_2 particles disperse evenly on the surface of RGO. The high-resolution TEM (HRTEM) image (Figure 3b) shows that MoS_2 nanoparticles lay flat on the RGO nanosheet, with highly exposed edges. The authors claimed that the strong chemical and electronic coupling between MoS_2 particles and RGO sheets is the key to the formation of highly dispersed, few-layered MoS_2 on RGO. Meanwhile, RGO not only acts as the supporting substrate but also affords a more rapid electron transport. Even though RGO is electrochemically inert, the substantially increased active edges and the high electrical conductivity of the MoS_2/RGO heterostructure eventually grant the superior catalytic activity (Figure 3c). In addition, the Tafel slope of the MoS_2/RGO heterostructure (41 mV dec^{-1}) was the smallest reported among MoS_2-based catalysts at that time (Figure 3d).

Similarly, mesoporous graphene foams (MGFs) were introduced for growing highly dispersed MoS_2 nanoparticles,[75] and MGFs served as nucleation sites and enabled the formation of ultrafine MoS_2 nanoparticles with an average size of 2 nm. Owing to the high specific surface area and interconnected conductive skeleton of MGFs, the obtained MoS_2/MGF heterostructure acquired high edge exposure, displaying a high apparent cathodic current density of 100 mA cm^{-2} at an overpotential of 200 mV. Additionally, anchoring heterostructures on macroscopic conductive substrates can further increase the exposure of active sites and facilitate mass transfer. For example, Cai et al. deposited Ni_2P nanosheets and graphene sheets on the surface of NF.[96] Benefiting from largely increased number of active sites and accelerated mass transfer, 3D Ni_2P/graphene/NF merely required a low overpotential of 75 mV to achieve a current density of 10 mA cm^{-2}.

Constructing heterostructures can also improve the stability of the catalyst, which is vital to the practical application of water electrolysis devices. For example, transition-metal-based catalysts are potential substitutes for noble metals, but most of these transition metals are prone to be corroded in acidic media. Deng et al. encapsulated Fe, Co, and FeCo alloy into N-doped CNTs (NCNTs) as shown in Figure 3e and f, and the FeCo@NCNTs heterostructure showed the highest HER activity (Figure 3g).[97] In addition, by increasing the amount of nitrogen in NCNTs, the obtained FeCo@NCNTs-NH heterostructure exhibited further promoted HER activity with an overpotential of ~280 mV at 10 mA cm^{-2}. The origins of the enhanced HER activity were investigated by DFT calculations, which proved that the introduction of metal and nitrogen could synergistically modulate the electronic structure of the CNTs and thus regulate the $\Delta G°_H$ of CNTs. Moreover, the FeCo@NCNTs heterostructure

acquired extraordinary stability in 0.1 M H_2SO_4 over 10000 CV cycles due to the protection of the carbon walls to these metal nanoparticles (Figure 3h). Later, few-layered graphene encapsulated transition metals were found to display similar behavior.[98] As illustrated in Figure 3i, the CoNi alloy particles were encapsulated in few layered graphene-spheres (CoNi@NC), which granted the CoNi@NC heterostructure long-term stability in 0.1 M H_2SO_4. Also, the heterostructure exhibited highly catalytic performance toward HER with an overpotential of 224 mV at 10 mA cm^{-2}. DFT calculations demonstrated that the electron of a CoNi cluster can penetrate through three graphene layers (Figure 3j), and this electron density redistribution together with the nitrogen dopants synergistically increase the electron density on the graphene surface, resulting in a higher proton affinity and the subsequent superior HER activity of the graphene shells.

Owing to the unique 2D nanostructure and high conductivity, graphene-based substrates (e.g., graphene, GO, and RGO) can serve as excellent supports for nanostructured HER catalysts. Hybridization with graphene-based supports has been proved to be extremely effective for a variety of highly active HER catalysts, such as FeP nanoparticles grown on graphene sheets,[37] $MoSe_2$ nanosheets on RGO sheets,[99] 2D WS_2 sheets on RGO,[100] $W_xMo_{1-x}S_2$/Graphene,[101] phosphorous-modified WN/RGO, [43] vertical-oriented WS_2 nanosheets on RGO,[102] N, S co-doped GO sheets decorated with CoP,[103] etc. Meanwhile, other carbonaceous substrates including CNTs,[55, 92, 104-106] activated carbon,[35, 107] are also employed to support advanced HER catalysts. In these carbonaceous material-supported heterostructures, the carbonaceous substrates may play a confinement role in the formation of well-dispersed nanostructures and the exposure of sufficient active sites for the HER. Besides,

these highly conductive carbonaceous supports easily afford fast electron transport, which is pivotal to achieving high catalytic activity. Moreover, other components in the heterostructures or the presence of heteroatom dopants may modulate the electronic structure of the carbonaceous supports, and thus activate their HER activity. As a result, growing active materials on carbonaceous supports is an effective approach to synthesizing advanced HER catalysts.

4.1.2 TMD/TMD heterostructures

Recently, earth-abundant TMDs have drawn considerable attention in electrochemical water splitting, including 2D layered TMDs (e.g. MoS_2, $MoSe_2$, WS_2, etc.) and cubic pyrite-type or orthorhombic marcasite-type TMDs (e.g. CoS_2, $CoSe_2$, NiS_2, FeS_2, etc.).[36, 108-112] Owing to the moderate hydrogen binding energy or the partially filled E_g band, these TMDs materials usually display high intrinsic HER activity. Interestingly, heterostructures formed by hybridizing different TMDs may exhibit even higher HER activities than their single counterparts.

Gao et al. prepared a highly active $MoS_2/CoSe_2$ heterostructure by coating the quasi-amorphous MoS_2 on the surface of $CoSe_2$/DETA nanobelts.[49] **Figure 4**a shows the evenly distributed MoS_2 nanosheets over the surface of $CoSe_2$/DETA nanobelts. The noble-metal-free heterostructure exhibits a substantial enhanced HER activity over $CoSe_2$ and MoS_2 in 0.5 M H_2SO_4, with a low overpotential of ~75 mV at 10 mA cm^{-2} (Figure 4b). The small Tafel slope of 36 mV dec^{-1} is comparable to the commercial Pt/C catalyst (30 mV dec^{-1}), suggesting a Tafel-step-determined Volmer-Tafel mechanism for the HER on the surface of the $MoS_2/CoSe_2$ heterostructure. DFT calculations based on Volmer-Tafel route further reveal

an activation barrier of 1.13 eV for the Tafel step on the $MoS_2/CoSe_2$ heterostructure (Figure 4c), approaching to that on Pt (111) electrode. The chemical binding between MoS_2 and $CoSe_2$ and the substantially increased number of active sites jointly account for the high intrinsic activity. Moreover, the $CoSe_2$/DETA nanobelts possess high conductivity and superior electrocatalytic activity, making $CoSe_2$/DETA nanobelt excellent support for growing TMD nanomaterials. A similar $CoS_2/CoSe_2$ heterostructure with well-dispersed CoS_2 nanoparticles distributed on the surface of $CoSe_2$/DETA was reported (Figure 4d),[113] exhibiting substantially improved HER activity (Figure 4e). X-ray photoelectron spectroscopy (XPS) spectra was employed to investigate the possible enhancement mechanism. As shown in Figure 4f and g, compared with their counterparts, the S 2p and Se 3d spectra of $CoS_2/CoSe_2$ heterostructures shift toward lower and higher binding energy, respectively. Generally, these variations in binding energies are interpreted as an indicator for electron transfer and/or chemical binding between different components of heterostructures.[113-115] However, deeper explanations regarding how the electron transfer affects HER activity are usually overlooked.

Zhou et al. reported a vertical $MoSe_2$/NiSe heterostructure and explored the XPS binding energy shift within the heterostructure.[58] Figure 4h demonstrates the epitaxial structure with well-defined interfaces along the vertical direction. In the XPS spectra (Figure 4i), the Mo 3d binding energy of the $MoSe_2$/NiSe heterostructure shift negatively compared with that of $MoSe_2$. As usual, an electron transfer from NiSe to $MoSe_2$ was proposed, which was further verified by electron energy loss spectroscopy (EELS) analysis. Moreover, ultraviolet photoelectron spectroscopy (UPS) spectra were obtained to calculate the valence band (E_v)

and the work function (φ) of $MoSe_2$ and NiSe. Figure 4j shows the schematic diagram of energy band alignment at the interface between $MoSe_2$ and NiSe deduced from the UPS results. The higher Fermi level of NiSe facilitates the electron injection form metallic NiSe into $MoSe_2$ (Figure 4k), which increases the conductivity of the $MoSe_2$/NiSe heterostructure.

Similar to carbonaceous material-supported heterostructures, these TMD/TMD heterostructures usually maintain plenty of active sites due to the well-established nanostructures.[49, 116] Besides, the synergistic effect and electron transfers between the different TMD components also contribute to the high HER activity.[58, 115, 117] Moreover, the HER activity of these TMD/TMD heterostructures can be further promoted by hybridizing with CNT, RGO, and CC, etc,[114, 118-119] which will not only further increase the number of active sites and the electrical conductivity but also enable rapid mass transportation.[120]

4.1.3 TMP-based heterostructures

In transition metal phosphides (TMPs), electrons tend to transfer from metal atoms to the more electronegative P atoms; thus, the negatively charged P atoms can efficiently trap protons during the HER process.[13] In 2005, Liu and Rodriguez employed DFT calculations to evaluate the HER on Ni_2P surfaces, and the results suggested that the energy variation of the HER on Ni_2P(001) surface was close to that on Pt(111) surface. The presence of P decreases the number of Ni sites and hence leads to a moderate binding of H* on the surface, making Ni_2P an excellent HER catalyst.[121] As expected, hybridizing TMPs with conductive supports is beneficial for increasing active sites and enhancing electrical conductivity,[122-123] and heteroatom doping may further promote the electrocatalytic performance.[124] Likewise, some TMP/TMP heterostructures are also reported.[125-126] Wang et al. constructed a 3D

self-supported Ni_5P_4-Ni_2P nanosheet arrays on NF via the direct phosphorization of commercially available NF using P vapor.[126] As shown in **Figure 5**a, the NF substrate affords a 3D porous skeleton for growing the Ni_5P_4-Ni_2P nanosheet arrays (Ni_5P_4-Ni_2P-NS), which not only increases the number of active sites but also facilitates the mass diffusion process. Due to the highly positively charged Ni and the strong ensemble effect of P, the Ni_5P_4 species acquire superior electrocatalytic activity. Further promoted by the synergistic effect between Ni_5P_4 and Ni_2P phases, the Ni_5P_4-Ni_2P-NS heterostructure merely require an overpotential of 120, 140, and 200 mV to drive a cathodic current density of 10, 20, 100 mA cm^{-2}, respectively (Figure 5b). The stability of the Ni_5P_4-Ni_2P-NF electrode was evaluated based on an accelerated degradation test (CV, -200~60 mV vs. RHE, 50 mV s^{-1}). After the accelerated degradation test, the overpotential only increases by 18 and 21 mV to achieve a current density of 10 and 100 mA cm^{-2}, respectively (Figure 5c). Further, the sheet-like morphology is preserved after the stability test, and only Ni and P exist in the cycled electrode. Tang et al. proposed a generally applicable synthesis routine for preparing heterostructures of phosphides, sulfides and selenides (Figure 5d).[127] Taking phosphides as an example, the Ni_2P/CoP/CC heterostructure that is composed of Ni_2P nanosheets on CoP nanowires supported on CC preserves well-constructed 3D architecture (Figure 5e), which facilitates the release of hydrogen gas and ensures sufficient active sites. The synergistic effect between Ni_2P and CoP further promotes the HER activity, resulting in a low overpotential of 55 mV at a current density of 10 mA cm^{-2} and a small Tafel slope of 48 mV dec^{-1}.

Alternatively, TMP-based heterostructures can be constructed by hybridizing TMPs with TMDs or carbides.[128-130] A CoP/MoS_2-CNTs hybrid catalyst was achieved via the *in situ*

growth of CoP on the surface of MoS_2-CNTs (Figure 5f).[131] The introduction of CNTs substantially increased the specific surface area and improved the electrical conductivity of the catalyst, both of which are crucial for the HER. The CoP/MoS_2-CNTs heterostructure displays an almost identical LSV curve to 20% Pt/C in 0.5 M H_2SO_4. Regmi et al. deposited phosphides of Ni, Fe, and Co on Mo_2C to generate nanocrystalline heterostructures.[132] The obtained phosphide/carbide composites exhibited both high HER catalytic activity and long-term stability. Detailed investigations on the used catalyst revealed that the lattice mismatch between the two components contributed to the improved electrochemical stability, and the FeP/Mo_2C with the lowest degree of lattice mismatch displayed the optimal stability.

In acidic solutions, the coordinated water molecules in hydronium ions will reduce the positive charge density of H^+ and hamper H^+ to receive electrons from the cathode,[133] resulting in large overpotential of HER on non-noble metal catalysts. Feng et al. reported a CF-supported polyaniline (PANI) nanodots (NDs)-decorated CoP hybrid nanowires (HNWs) heterostructure (PANI/CoP HNWs-CFs), as illustrated in Figure 5g, which exhibited Pt-like HER performance.[134] The amine groups in PANI can easily capture the H^+ in hydronium ions and thus eliminate the negative influence of hydronium ions caused by the binding water molecules. As a result, the PANI/CoP HNWs-CFs heterostructures demonstrate higher HER current density than commercial 20% Pt/C at relatively high overpotential (Figure 5h), where the dynamics behavior of H^+ capture is the key factor.

4.1.4 Transition-metal-oxide (TMO)-based heterostructures

In general, most TMOs are not favored for HER in acidic media because of the lack of adsorption sites for H* (e.g. TiO_2, MoO_3, WO_3, NiO, etc.),[68] and some TMOs may be

corroded in acidic solutions (e.g. CuO, Fe_2O_3, MoO_3, etc.). However, a few TMO-based heterostructures show attractive HER performance in acidic solutions. For example, vertically oriented MoO_3/MoS_2 nanowires were prepared via sulfuration at various temperatures,[135] and the core-shell structure is demonstrated in **Figure 6**a. Despite of the corrosion tendency of MoO_3 in 0.5 M H_2SO_4, the MoO_3/MoS_2 heterostructure exhibits an overpotential of ~250 mV at an current density of 10 mA cm^{-2} and remains good performance stability over 10000 CV cycles (Figure 6b). The MoO_3 nanowires served as a high aspect ratio substrate for growing MoS_2 and enabled facile charge transport. In the meantime, the MoS_2 shell prevented the MoO_3 core from the direct contact with the corrosive electrolyte. The HRTEM image in Figure 6c demonstrates the well-preserved core-shell structure, ensuring the excellent stability of the MoO_3/MoS_2 heterostructure in acidic media. Likewise, Yang et al. reported a MoS_2/MoO_2 heterostructure obtained by sulfuration treatment of porous and highly conductive MoO_2.[53] The catalyst showed an overpotential of 240 mV at 10 mA cm^{-2}, a Tafel slope of 76.1 mV dec^{-1}, and robust durability. The high electrical conductivity promotes the rapid electron transport while the porous structures facilitate fast mass diffusion. There are a variety of TMO-based heterostructures reported as electrocatalysts for acidic HER.[63, 136-139] Most of them possess core-shell structures with a TMO core and a HER-active shell (Figure 6d~i), in which the active shell will shield the TMO core from corrosion, resulting in improved durability. On the other hand, many reports ascribe the enhanced HER activity to the high electrical conductivity of the TMO core. For example, the typical electrical conductivity of MoS_2 is 10^{-4}~10^{-5} S cm^{-1} while the electrical conductivity of MoO_2 can reach as high as 10^2~10^3 S cm^{-1}.[140-141] The highly conductive MoO_2 core enables fast electron

transport in the MoS_2/MoO_2 heterostructure, and hence a higher HER activity. However, many TMOs (e.g., MoO_3, SnO_2) are not good conductive material, yet the high HER activity of these TMO-based heterostructures are still ascribed to the "highly conductive TMO core". Moreover, the electric conductivity is related to the dimension and morphology.[142-143] Hence, it is highly desirable to provide sufficient supporting evidence when discussing the electrical conductivity.

4.1.5 Noble-metal-based heterostructures

To date, noble metals such (e.g., Pt, Pd) and their alloys are still the most active HER catalysts, but the elemental scarcity of the noble metals severely increases the catalyst cost. Therefore, intensive research attention is focused on developing low-cost alternatives to noble metal-based catalysts. There is also an argument that the elemental scarcity of Pt is not so severe as it is supposed to be.[144] Instead, many noble metal-free catalysts such as cobalt-based and molybdenum-based materials might be even more scarce since much higher catalyst loading is required to achieve the same current density with that of using Pt. Nevertheless, constructing noble-metal-based heterostructures could further explore the activity limit of noble metals and make noble-metal-based catalysts more affordable.

Sengeni et al. anchored ultrafine Pt particles on DNA molecules,[145] with Pt particles uniformly distributed on the surface of DNA molecules, as demonstrated in **Figure 7**a. The high electrochemical stability and the excellent adhesion of DNA molecules to GC electrode enable them as excellent supports for Pt nanoparticle. As a result, the Pt/DNA heterostructure with Pt content of as low as 15 μg cm^{-2}, shows superior HER activity than the commercial 10% Pt/C catalyst in 0.5 M H_2SO_4. Meanwhile, the Pt/DNA heterostructure without binder

delivered stable electrocatalytic performance over 5000 CV cycles (Figure 7b). Moreover, the stability of the Pt/DNA catalyst was further checked by soaking the electrode in H_2 saturated 0.5 M H_2SO_4 solution for more than 10 days. Remarkably, the ultrafine Pt particles still show evident lattice fringe after the aging test (Figure 7c), highlighting the durability of the Pt/DNA heterostructure. Similar to Pt, metallic Rh is also an excellent HER catalyst. Hybridizing metallic Rh with HER-active MoS_2 nanosheets highly enhanced the HER activity of Rh.[146] Figure 7d displayed that the Rh nanoparticles have an average particle size of ~6 nm and dispersed evenly on the surface of MoS_2. The mass loading of Rh is as low as 5.2 wt% in the Rh-MoS_2 heterostructure, but the catalyst show a HER activity comparable to the 20 wt% Pt/C electrode (Figure 7e). On the other hand, the 5.2 wt% Rh-MoS_2 hybrid catalyst exhibits extraordinary mass activity of 13.87 A mg_{metal}^{-1} at an overpotential of 250 mV, which is four times as large as that of the commercial 20 wt% Pt/C catalyst. The superior performance was ascribed to the synergistic effect between Rh and MoS_2. As illustrated in Figure 7f, H_3O^+ are fast captured by the strong H^- adsorbed component Rh to become the adsorbed H atoms, which subsequently migrate to the surface of quick H_2-desorbed MoS_2 and finally released as hydrogen gas.

To date, various types of noble-metal-based heterostructures have been reported (Figure 7g~j), but the most active ones are still based on Pt or Pd, which possess the optimal binding energy to hydrogen.[147-153] The concept here is to make the full use of noble metals and taking advantage of the synergistic effect between the counterparts. Moreover, owing to the superior electrochemical stability of noble metals as well as the well-designed nanostructures, these noble-metal-based heterostructured catalysts are more likely to show long-term stability.

4.1.6 Other heterostructured catalysts

During the pursuit of highly active, cost-effective, and long-lasting catalysts for HER, transition metal carbides (TMCs) and transition metal nitrides (TMNs) also draw much attention due to their elemental abundance and catalytic properties.[154-155] It has been disclosed that introducing carbon into the lattices of non-noble metals will endow them with a higher d-band electronic density of states (DOS) at the Fermi level, and hence high catalytic activities.[154, 156] Tungsten carbides including WC and WC_2 have been explored as promising electrocatalysts.[157] However, most of the reported HER activities of tungsten-carbide-based catalysts are still much inferior to noble metals. An important reason is that the carbides are conventionally prepared by the reduction of metal precursors at high temperature, which easily results in uncontrollable morphology. Wang et al. synthesized a Ravenala leaf-like W_xC/WS_2 heterostructure with W_xC "leaves" attached to the WS_2 tubes via *in situ* carbonizing WS_2 nanotubes.[59] The hybrid electrode composed of $W_xC@WS_2$ heterostructure on carbon fibers shows an overpotential of 146 mV at 10 mA cm^{-2} and a Tafel slope of 61 mV dec^{-1}, outperforming either the bare WS_2 nanotubes or the W_xC counterpart (**Figure 8**a). Figure 8b shows the free energy diagrams of catalysts under different H* coverage along the reaction coordinate, and the results demonstrate that W_xC species bind H atoms too tightly while WS_2 bind H atoms too weakly. Interestingly, DFT calculations revealed an apparent electron transfer from the outmost W of W_2C to WS_2 (Figure 8c). This electron redistribution subsequently modified the d-band electronic DOS around the Fermi level, leading to a more close-to-neutral $\Delta G°_H$ for the $W_xC@WS_2$ heterostructure. Another challenge for tungsten carbides is the lack of methods to selectively synthesize different phases. Gong et al.

developed a two-step approach and successfully prepared the pure phase W_2C on multi-walled CNTs (MWNTs).[105] The ultrasmall W_2C nanoparticles are anchored on the outer walls of the MWNTs (Figure 8d), achieving a current density of 10 mA cm^{-2} at an overpotential of 123 mV (Figure 8e). Meanwhile, owing to the structural and electrochemical robustness, the heterostructure exhibited excellent stability with less than 10 mV increase in the overpotential at 10 mA cm^{-2} after 10000 continuous CV cycles (Figure 8f).

TMNs are also potential substitutes for noble metals. Yan et al. prepared a P-modified WN/RGO (P-WN/RGO) heterostructure via the phosphorization of WN/GO heterostructure.[43] Figure 8g shows that WN particles are evenly distributed on RGO surface. XPS revealed an electron transfer from P to WN, and the charge redistribution increased the electron density of the catalyst surface which subsequently promoted the HER activity. Kumar et al. hybridized γ-Mo_2N with β-Mo_2C on a carbon support. Figure 8h clearly shows the interface between γ-Mo_2N and β-Mo_2C. Interestingly, theoretical calculations demonstrated that the electron redistribution between the carbon supports and the active materials (γ-Mo_2N, β-Mo_2C) yielded active catalytic sites on the carbon layers. Also, the free energy profile of the HER on the heterostructure was demonstrated to be close to that on commercial Pt/C electrode (Figure 8i). As a result, the required overpotential to drive a current density of 10 mA cm^{-2} was only 96 mV.

4.2 Heterostructured catalysts for HER in alkaline media

4.2.1 Carbonaceous material-supported heterostructures

Not surprisingly, anchoring HER active materials on carbonaceous substrates also works for synthesizing efficient catalysts for the alkaline HER. By simultaneously depositing Ni

nanoparticles and RGO sheets on NF,[158] the obtained Ni-based catalyst required only 36 mV to achieve a current density of 10 mA cm^{-2} in 1 M NaOH. The high conductivity of both RGO and NF jointly contribute to fast electron transport. Meanwhile, the 3D architecture of NF can accelerate the mass transportation and increase the surface area of the electrode. In addition, the introduction of RGO sheets strengthened the exposure of (111) crystal planes of Ni, which granted the high intrinsic activity. The carbonaceous supports can also protect the active material from the alkaline solutions. For instance, carbides usually exhibited poor stability in neutral or higher pH solutions.[159] However, a carbon-protected bimetallic Co-W carbide catalyst kept stable at a large current density (> 30 mA cm^{-2}) in 1 M KOH for as long as 18 h.[160] Su et al. encapsulated Ru and Co bimetallic nanoalloy within N-doped graphene layers (RuCo/NC) through a one-step process by annealing Ru-doped Prussian blue analogues.[161] The amount of Ru in the catalyst was only 3.5 wt %, yet the catalyst delivered highly active HER performance in 1 M KOH with an overpotential of 28 and 218mV at 10 and 100 mA cm^{-2}, respectively. Due to the protection of the graphene layers to the metal nanoalloy, the RuCo/NC heterostructure maintained high activity over 10000 CV cycles.

Similar to the cases in acidic media, the enhanced alkaline HER activity of these carbonaceous material-based heterostructures may originate from the high conductivity, fully exposed active sites, as well as synergistic effects between counterparts. Therefore, many carbonaceous material-supported heterostructures are more likely to show high HER activity in both alkaline media as well as acidic solutions.[162-163] Although the water dissociation process is the dominating issue for alkaline HER, few reports claim that the water dissociation step is accelerated in carbonaceous material-supported heterostructures. The reason might be

that carbonaceous materials are usually not favored by water adsorption. DFT calculations showed that the water adsorption energy is 0.35 eV on MWCNT,[164] -0.1 eV on graphite,[165] and ~0.1eV on graphene.[166]

4.2.2 Transition-metal-hydroxide-based heterostructures

As described in previous sections, promoting the water dissociation step is a fruitful approach to designing advanced catalyst for alkaline HER. Recently, some studies have demonstrated that transition metal hydroxides such as $Ni(OH)_2$, $Co(OH)_2$, and $Ni_xFe_y(OH)_2$ were effective promoters for water dissociation.

Subbaraman et al. modified Pt electrode with $Ni(OH)_2$ nanoclusters and studied the promotion effect of $Ni(OH)_2$ on HER activity.[61] Scanning tunneling microscopy (STM) image in **Figure 9**a shows the surface morphology of the $Ni(OH)_2$ nanocluster-modified Pt(111)/Pt-islands (ad-islands) electrode. The presence of Pt-islands increases the active sites. After the modification with $Ni(OH)_2$, the Pt(111)/$Ni(OH)_2$ electrode exhibits further enhanced HER activity (Figure 9b). The authors believed that the water adsorption process was accelerated by the simultaneous interaction of O atoms with $Ni(OH)_2$ and H atoms with Pt at the boundary between $Ni(OH)_2$ and Pt domains. Therefore, with the accelerated water dissociation by $Ni(OH)_2$ nanoclusters, the generated hydrogen intermediates were subsequently adsorbed on the nearby Pt surfaces and finally recombined into H_2 (Figure 9c). Moreover, introducing Li^+ further enhanced the generation of the hydrogen intermediates due to the destabilization effect of Li^+ on the HO-H bond. Soon later, Danilovic et al. systematically studied the HER performance of a variety of $Ni(OH)_2$-modified metal electrodes.[62] The results summarized in Figure 9d show that $Ni(OH)_2$ can faciliate HER on

the surface of almost all metals. The promotion was ascribed to a synergistic effect between $Ni(OH)_2$ and metals where $Ni(OH)_2$ facilitate the water dissociation, and the generated hydrogens were subsequently adsorbed and associated on metal surfaces. In 2017, Yu et al. studied the relationship between the promoted alkaline HER activity and the structure of $Ni(OH)_2$ by loading α-$Ni(OH)_2$ and β-$Ni(OH)_2$ on Pt electrode.[167] Both experimental and theoretical results proved that β-$Ni(OH)_2$ was a better promoter for the alkaline HER on Pt due to the higher water dissociation ability and stronger interactions between β-$Ni(OH)_2$ and Pt.

Transition metal hydroxides were also found to be able to enhance alkaline HER kinetics on various type of catalysts including TMDs, TMPs, and nitrides. For example, Zhang et al. reported a 3D $Ni(OH)_2/MoS_2$/CC heterostructure with nano-sized $Ni(OH)_2$ particles are anchored on the surface of MoS_2 (Figure 9e).[168] The $Ni(OH)_2/MoS_2$/CC heterostructures achieve an substantial enhanced HER activity in 1 M KOH with an overpotential of 80 mV at 10 mA cm^{-2} (Figure 9f). DFT calculations revealed the H_2O adsorption energy is 0.05 eV for the heterostructures, in sharp contrast to 1.17 eV for MoS_2. The free energy diagrams of the HER process on the surface of $Ni(OH)_2$, MoS_2 and the heterostructure obtained from DFT calculation are displayed in Figure 9g. The results proved a large decrease in the free energy of both water dissociation and hydrogen adsorption on the surface of the $Ni(OH)_2/MoS_2$ heterostructure. Chen et al. reported a $Ni(OH)_2/CoS_2$/CC nanowire array with substantially enhanced HER activity (Figure 9h).[60] DFT calculations revealed a similar decrease in the free energy of the HER on the $Ni(OH)_2$ modified electrode. Other transition-metal-hydroxide-based heterostructures for the alkaline HER include

NiCo-LDH/MoS_2,[169] $Ni(OH)_2$/1T-MoS_2,[170] $Ni(OH)_2$/CuS core-shell heterostructures,[171] $Ni(OH)_2$/Ni3N/TM nanoarrays,[172] $Ni(OH)_2$-Fe_2P/TM,[173] $Ni(OH)_2$-PtO_2/TM[174], etc. Also, transition metal hydroxides can be used as a substrate for growing alkaline HER catalysts. Xing et al. designed CC supported $Co(OH)_2$ nanosheets array as a 3D substrate for electrodepositing ultrafine Pt nanoparticles (Figure 9i, j).[175] Yin et al. synthesized ultrathin Pt nanowires (NWs) on single-layered (SL) $Ni(OH)_2$ (Figure 9k, l).[176] Both of these heterostructures showed superior HER performance over the commercial Pt/C electrode due to the accelerated water dissociation process. These results proved the ability of transition metal hydroxides in accelerating water adsorption and water dissociation process, which would be effective in designing advanced alkaline HER catalysts.

4.2.3 TMO-based heterostructures

The superior HER performance of transition-metal-hydroxide-based heterostructures has demonstrated the efficiency of regulating water dissociation sites for constructing advanced alkaline HER catalysts. According to several relevant studies,[177-179] strong interactions between the adsorbed H_2O species and oxide surfaces are expected, which may grant TMOs the ability to promote the water dissociation step in alkaline HER. For example, Gong et al. reported a nanoscale NiO/Ni-CNT heterostructure with a substantially enhanced alkaline HER activity due to the promotion of NiO species to the water dissociation step. The NiO/Ni-CNT heterostructure was synthesized by annealing $Ni(OH)_2$ precursor bonded on CNT sidewalls at 300 °C in Ar flow.[180] The HRTEM image in **Figure 10**a and the corresponding EDX mapping image in Figure 10b clearly reveal the core-shell structure with a NiO shell over Ni particle core. The obtained NiO/Ni-CNT heterostructure exhibited superior HER activity than

both NiO/CNT and Ni/CNT (Figure 10c). The high HER activity was believed to be originated form the synergistic effect between NiO and Ni species, and the exposed NiO/Ni interfaces at the discontinuity of the NiO shell were believed to be the synergistically active sites. The activity of the pure Ni surface is low in alkaline media because OH^- could occupy the sites for H adsorption; while the NiO surface is not active for the HER because of the lack of H adsorption sites. However, in the NiO/Ni-CNT heterostructure, OH^- could preferentially attach to NiO site at the heterojunction because of the strong electrostatic attraction of Ni^{2+} to OH^-; meanwhile, H^+ can adsorb at a nearby Ni site. Besides, the presence of CNT can prevent the agglomeration of nanoparticles as well as ensure a good electrical conductivity. Consequently, the introduction of CNT and the synergistic effect between NiO and Ni endow the NiO/Ni-CNT heterostructure a substantially enhanced HER activity in alkaline solution.

A similar 3D Co/Co_3O_4 core-shell heterostructure was achieved by reducing *in situ* grown Co_3O_4 nanosheets at 200 °C in a hydrogen atmosphere.[50] Figure 10d demonstrates the well-preserved nanosheets morphology, and the core-shell structure with an amorphous Co_3O_4 shell over the metallic Co core can be revealed by the TEM image in Figure 10e. A low overpotential of ~90 mV at 10 mA cm^{-2} is achieved in 1 M KOH (Figure 10f). The amorphous Co_3O_4 shell was believed to facilitate the dissociation of water by promoting the activation of Lewis basic H_2O through Lewis acid-base interaction. Besides, oxygen vacancies also play a significant role in enhancing the adsorption of water since the oxygen-vacancy-bearing oxide possesses a more positive potential on the surface. Further, the well-constructed 3D structure facilitates the mass transportation and the highly conductive metallic Co core grants the fast electron transfer process. Weng et al. reported a Ni/CeO_2 heterostructure on the surface of

CNTs.[181] The interfaces between Ni and CeO_2 nanoparticles are clearly displayed in Figure 10g. As demonstrated by DFT calculations, the Ni/CeO_2 interfaces not only facilitates the dissociation of water molecules but also lowers $\Delta G°_H$ to the same level of Pt (Figure 10h). Further, a CoP/CeO_2 heterostructure on TM (Figure 10i, j),[182] a CeO_2/Cu_3P nanoarray supported on N,[183] were reported with a remarkable HER activity in 1 M KOH. DFT calculations suggested the heterostructure possesses a lower water dissociation free energy and a more optimal hydrogen adsorption free energy than their counterparts. Other TMOs including MoO_3 (Figure 10k, l),[184] PtO_2,[185] TiO_2,[186] etc., were also reported towards promoting the alkaline HER activity. As previously mentioned, TMOs are usually used in acidic media as the conductive core in core/shell structures and are protected by other HER-active components. In contrast, TMOs can directly contact with alkaline solutions, either anchoring on the surface of other components or serving as shells or substrates. The principal objective here is to accelerate the water dissociation process by the incorporation of TMO species.

4.2.4 Metal-based heterostructures

Compared to that in acidic media, most transition metals are relatively stable in alkaline solutions, acting as potential alkaline HER catalysts. For example, nickel is a popular choice for alkaline water electrolysis due to low cost, high activity, and excellent resistance to corrosion in concentrated alkaline solutions.[187-188] After the first report in the early 1900s, tremendous efforts have been devoted to understanding the catalytic mechanism of Ni.[158, 189-191] Zhang et al. reported Ag/Ni core-shell heterostructures (**Figure 11**a) which showed substantially improved HER activity over the bare Ni or Ag (Figure 11b) in 0.1 M KOH.[192]

As the best conductive metal, silver provides super-fast electron transportation pathway in the heterostructures. However, adding too much nickel will block the Ag nanowires and decrease the number of bimetallic interfaces, resulting in a decreased HER performance. Hence, the synergistic effect between Ni and Ag was crucial for the enhanced HER activity. Deng et al. engineered the catalyst/electrolyte interface by introducing Pd during the formation of $Ni@Ni(OH)_2$ heterostructure. SEM image in Figure 11c shows that $Ni@Ni(OH)_2$ particles are freely grown on RGO surface with an average diameter of 200 nm. As displayed in Figure 11d, the presence of Pd seeds substantially facilitate the grain refinement and the dispersion of the homogeneous-sized $Ni@Ni(OH)_2$/Pd particles (~10 nm). Thus, significantly enhanced HER activity over the $Ni@Ni(OH)_2$/RGO without Pd can be achieved by the $Ni@Ni(OH)_2$/Pd/RGO heterostructures (Figure 11e).

Although Pt exhibits inferior HER performance in alkaline media comparing with acidic solutions, it still maintains a competitive edge due to its high intrinsic activity. Interestingly, introducing Pt into the heterostructures can modify the catalyst/electrolyte interface. For instance, a 3D Ni electrode with a Pt-modified surface showed substantial enhancement in HER activity.[193] The Pt loading was as low as 0.5 mg cm^{-2} and 50 μg cm^{-2} based on the geometric surface area and the specific surface area, respectively. Also, constructing heterostructures also helps to achieve a high exposure of Pt. He et al. deposited Pt particles on the surface of RuO_2-TiO_2 (RTO), as shown in Figure 11f. Due to the confinement effect of the RTO substrate, the Pt particles display an average particle size of 6 nm. Although the commercial Pt/C catalyst has a smaller particle size (~ 2.5 nm), the Pt/RTO heterostructure exhibited higher HER activity with an exchange current density of 2.31 ± 0.06 mA cm^{-2}_{pt} in

0.1 M KOH, which is five times that of the 46.5% Pt/C catalyst.[194] The reason for this dramatic enhancement could be ascribed to the presence of oxygen vacancies in RuO_2, which promoted the water dissociation step and thus largely reduced the activation energy for the HER process. Further, the Pt/RTO catalyst was employed in a solid-alkaline water electrolyzer. The results showed the Pt/RTO cathode was more efficient than 46.5% Pt/C for hydrogen production, and a reduction of 100 ~ 200 mV in the overpotential was observed across the entire current density range when compared with commercial Pt/C.

4.2.5 Other heterostructured catalysts

There are also TMD/TMD heterostructures reported for alkaline HER, including interlaced NiS_2/MoS_2 nanoflake-nanowires,[195] heteromorphic $NiCo_2S_4/Ni_3S_2$/NF,[196] $NiMo_3S_4/Ni_3S_2$,[197] 3D $MoSe_2@Ni_{0.85}Se$ nanowire networks,[198] and most of these research ascribe the enhanced HER activity to the massive exposed active sites, interfacial interactions, and the 3D porous conductive substrates. In addition to LDHs and TMOs, some TMDs are also favored for water adsorption process, which could be used as water adsorption/dissociation promoters. DFT calculations demonstrated that the water adsorption energy on the surface of orthorhombic-phase $CoSe_2$ (o-$CoSe_2$) and cubic-phase $CoSe_2$ (c-$CoSe_2$) are -0.106 and -0.163 eV, respectively.[199] Inspired by the unique water adsorption capability, Zhao et al. synthesized $CoSe_2/MoSe_2$ heterostructures with c-$CoSe_2$ quantum dots anchored on $MoSe_2$ nanosheets (**Figure 12**a), which exhibited much higher HER activity than bare $MoSe_2$ nanosheets in 1 M KOH.[200] Figure 12b displays the LSV polarization curves of the catalysts. For the $CoSe_2/MoSe_2$ heterostructures, the optimal overpotential required to reach a current density of 10 mA cm^{-2} is merely 218 mV, more than 100mV lower than $MoSe_2$.

Meanwhile, as shown in Figure 12c, the TOF of $CoSe_2$/$MoSe_2$ heterostructures increased dramatically, demonstrating the substantial increment of the intrinsic activity which is originated from the synergistic effect between $CoSe_2$ and $MoSe_2$.

Besides, some heterostructured carbides, nitrides and phosphides materials also demonstrated excellent HER activity in alkaline media.[201-203] Xing et al. reported a self-standing Ni-WN heterostructure nanowire arrays supported on CC, and corresponding TEM and HRTEM images of the heterostructure are shown in in Figure 12d-f.[204] As a hydrogen-evolving cathode in 1.0 M KOH, this Ni-WN/CC electrode exhibited a lower overpotential than either WN/CC or Ni/CC due to the electrocatalytic synergistic effect of Ni and WN.

5. Conclusions and perspectives

Electrochemical water splitting driven by sustainable energies plays an indispensable role in making a hydrogen economy become a reality, and developing cost-effective catalysts with high activity and long-term durability is crucial for realizing economic hydrogen production. In this review, we summarized the state-of-the-art research progress on heterostructured catalysts for HER in acidic and alkaline media, with focuses on material design and synthesis strategies, electrochemical performance as well as the related mechanisms of activity enhancement. In general, the superior HER catalytic performance of the heterostructured catalysts can be attributed to the increased number of active sites, the improved intrinsic activity, or the accelerated mass and charge transfer process, all of which are more or less closely associated with the surface/interface tuning, the electronic structure modulation, the synergistic effect between the components, and so forth.

Electrochemical water splitting is a very appealing research area, and there have been enormous research advances regarding new catalyst development recently. When we look at the ever-increasing research progress, it can be found that the catalytic performance of the catalysts varies very significantly even for catalysts with similar composition and nanostructures. The electrochemical testing and performance description protocols should be unified, and sufficient details should be provided when discussing catalytic performance to avoid delivering ambiguous or inexact information. For example, the non-Faradic current should be subtracted when using macroscopic porous substrates, and the corresponding overpotential as well as the method for evaluating active sites should be indicated when discussing TOFs. With regard to the practical application of electrochemical HER catalysts, the scale-up synthesis of catalysts is a big obstacle and most synthesis processes are still restricted to laboratory level, although many heterostructured catalysts show exceptional activity and meet the performance demand of practical applications. Therefore, developing cost-effective and scalable synthesis strategies is one of the top challenges for practical heterostructured catalysts. Meanwhile, the performance stability is another crucial aspect. Despite of the high catalytic activities they may achieve, the catalytic activity of many heterostructured catalysts degrade quickly and the inferior performance stability severely restricted their application in water electrolysis devices. Besides, most reports merely investigate the performance durability under working conditions, but the performance degradation mechanisms are rarely studied. Therefore, more specific efforts should be devoted to establishing effective approaches to unravel the intrinsic reasons for activity degradation. Developing *in-situ/operando* high-resolution characterization methodologies is

vital to gain in-depth understanding of the degradation mechanism and the structure-composition-performance relationship, and this will provide new advanced knowledge for rational design of robust catalysts. Another challenging topic is about "synergistic effect", which is very frequently mentioned to interpret the superior catalytic activity of heterostructured catalysts. However, it has to be noted that the real synergistic effect in various heterostructured catalysts is not yet fully understood and should be further explored in the future work. More solid evidences should be acquired to clarify what the real synergistic effect is and how it works to make the catalysts deliver enhanced catalytic activity. In addition, a combination of theoretical and experimental work is also of great significance to gain more fundamental insights and to achieve intelligent design of heterostructured catalysts. Overall, we believe that, constructing well-defined heterostructures is one very promising and challenging strategy to design highly efficient catalysts for electrochemical water splitting, and the rapid development of renewable energy-drived electrochemical water electrolysis will light up the future of hydrogen economy.

Acknowledgements
This work was financially supported by the Australian Research Council (ARC) DECRA Grant (DE160100596) and AIIM FOR GOLD Grant (2017, 2018).

Received: ((will be filled in by the editorial staff))
Revised: ((will be filled in by the editorial staff))
Published online: ((will be filled in by the editorial staff))

References

[1] S. Chu, A. Majumdar, *Nature* **2012**, *488*, 294.

[2] International Energy Agency, World Energy Outlook 2017, https://webstore.iea.org/world- energy-outlook-2017, accessed: May, 2018

[3] Q. Cheng, H. Yi, *Renewable Sustainable Energy Rev.* **2017**, *67*, 683.

[4] C. Binz, J. Gosens, T. Hansen, U. E. Hansen, *World Development* **2017**, *96*, 418.

[5] L. Schlapbach, A. Züttel, *Nature* **2001**, *414*, 353.

[6] C. C. McCrory, S. Jung, I. M. Ferrer, S. M. Chatman, J. C. Peters, T. F. Jaramillo, *J. Am. Chem. Soc.* **2015**, *137*, 4347.

[7] M. Carmo, D. L. Fritz, J. Mergel, D. Stolten, *Int. J. Hydrogen Energy* **2013**, *38*, 4901.

[8] I. Roger, M. A. Shipman, M. D. Symes, *Nat. Rev. Chem.* **2017**, *1*, 0003.

[9] G. W. Crabtree, M. S. Dresselhaus, M. V. Buchanan, *Physics Today* **2004**, *57*, 39.

[10] W. Kreuter, H. Hofmann, *Int. J. Hydrogen Energy* **1998**, *23*, 661.

[11] C. A. Grimes, O. K. Varghese, S. Ranjan, *Light, water, hydrogen: the solar generation of hydrogen by water photoelectrolysis*, Springer **2008**

[12] J. A. Turner, *Science* **2004**, *305*, 972.

[13] Y. Shi, B. Zhang, *Chem. Soc. Rev.* **2016**, *45*, 1529.

[14] S. Y. Tee, K. Y. Win, W. S. Teo, L. D. Koh, S. Liu, C. P. Teng, M. Y. Han, *Adv Sci (Weinh)* **2017**, *4*, 1600337.

[15] A. Konieczny, K. Mondal, T. Wiltowski, P. Dydo, *Int. J. Hydrogen Energy* **2008**, *33*, 264.

[16] J. Turner, G. Sverdrup, M. K. Mann, P. C. Maness, B. Kroposki, M. Ghirardi, R. J. Evans, D. Blake, *Int. J. Energy Res.* **2008**, *32*, 379.

[17] P. Wang, X. Zhang, J. Zhang, S. Wan, S. Guo, G. Lu, J. Yao, X. Huang, *Nat. Commun*

2017, *8*, 14580.

[18]J. Lim, D. Park, S. S. Jeon, C.-W. Roh, J. Choi, D. Yoon, M. Park, H. Jung, H. Lee, *Adv. Funct. Mater.* **2018**, *28*, 1704796.

[19]J. Ying, G. Jiang, Z. P. Cano, L. Han, X.-Y. Yang, Z. Chen, *Nano Energy* **2017**, *40*, 88.

[20]L. Zhang, L. Han, H. Liu, X. Liu, J. Luo, *Angew. Chem. Int. Ed.* **2017**, *56*, 13694.

[21]Y. Zhang, Q. Zhou, J. Zhu, Q. Yan, S. X. Dou, W. Sun, *Adv. Funct. Mater.* **2017**, *27*, 1702317.

[22]H. Fan, H. Yu, Y. Zhang, Y. Zheng, Y. Luo, Z. Dai, B. Li, Y. Zong, Q. Yan, *Angew. Chem.* **2017**, *129*, 12740.

[23]J. X. Feng, L. X. Ding, S. H. Ye, X. J. He, H. Xu, Y. X. Tong, G. R. Li, *Adv. Mater.* **2015**, *27*, 7051.

[24]H. Cheng, C.-Y. Su, Z.-Y. Tan, S.-Z. Tai, Z.-Q. Liu, *J. Power Sources* **2017**, *357*, 1.

[25]G. F. Chen, T. Y. Ma, Z. Q. Liu, N. Li, Y. Z. Su, K. Davey, S. Z. Qiao, *Adv. Funct. Mater.* **2016**, *26*, 3314.

[26]H. Cheng, Y.-Z. Su, P.-Y. Kuang, G.-F. Chen, Z.-Q. Liu, *J. Mater. Chem. A* **2015**, *3*, 19314.

[27]D. Yan, Y. Li, J. Huo, R. Chen, L. Dai, S. Wang, *Adv. Mater.* **2017**, *29*, 1606459.

[28]A.-L. Wang, H. Xu, G.-R. Li, *ACS Energy Lett.* **2016**, *1*, 445.

[29]D. Voiry, H. Yamaguchi, J. Li, R. Silva, D. C. Alves, T. Fujita, M. Chen, T. Asefa, V. B. Shenoy, G. Eda, M. Chhowalla, *Nat. Mater* **2013**, *12*, 850.

[30]Y. Kim, D. H. Jackson, D. Lee, M. Choi, T. W. Kim, S. Y. Jeong, H. J. Chae, H. W. Kim, N. Park, H. Chang, *Adv. Funct. Mater.* **2017**, *27*, 1701825.

[31]C. Xu, S. Peng, C. Tan, H. Ang, H. Tan, H. Zhang, Q. Yan, *J. Mater. Chem. A* **2014**, *2*, 5597.

[32]C. Ouyang, X. Wang, S. Wang, *Chem. Commun.* **2015**, *51*, 14160.

[33]L. Tao, X. Duan, C. Wang, X. Duan, S. Wang, *Chem. Commun.* **2015**, *51*, 7470.

[34]J.-X. Feng, J.-Q. Wu, Y.-X. Tong, G.-R. Li, *J. Am. Chem. Soc.* **2018**, *140*, 610.

[35]D. Y. Chung, S. W. Jun, G. Yoon, H. Kim, J. M. Yoo, K. S. Lee, T. Kim, H. Shin, A. K. Sinha, S. G. Kwon, K. Kang, T. Hyeon, Y. E. Sung, *J. Am. Chem. Soc.* **2017**, *139*, 6669.

[36]J. Zhang, T. Wang, P. Liu, S. Liu, R. Dong, X. Zhuang, M. Chen, X. Feng, *Energy Environ. Sci.* **2016**, *9*, 2789.

[37]Z. Zhang, B. Lu, J. Hao, W. Yang, J. Tang, *Chem Commun (Camb)* **2014**, *50*, 11554.

[38]A.-L. Wang, J. Lin, H. Xu, Y.-X. Tong, G.-R. Li, *J. Mater. Chem. A* **2016**, *4*, 16992.

[39]C. Wan, Y. N. Regmi, B. M. Leonard, *Angew. Chem.* **2014**, *126*, 6525.

[40]H. Ang, H. T. Tan, Z. M. Luo, Y. Zhang, Y. Y. Guo, G. Guo, H. Zhang, Q. Yan, *Small* **2015**, *11*, 6278.

[41]H. Ang, H. Wang, B. Li, Y. Zong, X. Wang, Q. Yan, *Small* **2016**, *12*, 2859.

[42]W. F. Chen, K. Sasaki, C. Ma, A. I. Frenkel, N. Marinkovic, J. T. Muckerman, Y. Zhu, R. R. Adzic, *Angew. Chem. Int. Ed.* **2012**, *51*, 6131.

[43]H. Yan, C. Tian, L. Wang, A. Wu, M. Meng, L. Zhao, H. Fu, *Angew. Chem. Int. Ed.* **2015**, *54*, 6325.

[44]H. Lin, Z. Shi, S. He, X. Yu, S. Wang, Q. Gao, Y. Tang, *Chem. Sci.* **2016**, *7*, 3399.

[45]D. Wang, Q. Li, C. Han, Z. Xing, X. Yang, *ACS Cent. Sci.* **2017**, *4*, 112.

[46]K. Rui, G. Zhao, Y. Chen, Y. Lin, Q. Zhou, J. Chen, J. Zhu, W. Sun, W. Huang, S. X. Dou,

Adv. Funct. Mater. 1801554.

[47] S. Dou, J. Wu, L. Tao, A. Shen, J. Huo, S. Wang, *Nanotechnology* **2015**, *27*, 045402.

[48] Y. Chen, Q. Zhou, G. Zhao, Z. Yu, X. Wang, S. X. Dou, W. Sun, *Adv. Funct. Mater.* **2018**, *28*, 1705583.

[49] M. R. Gao, J. X. Liang, Y. R. Zheng, Y. F. Xu, J. Jiang, Q. Gao, J. Li, S. H. Yu, *Nat. Commun.* **2015**, *6*, 5982.

[50] X. Yan, L. Tian, M. He, X. Chen, *Nano Lett.* **2015**, *15*, 6015.

[51] W. R. Frensley, *Heterostructures and Quantum Devices, Academic Press, New York* **1994**.

[52] R. D. Nikam, A. Y. Lu, P. A. Sonawane, U. R. Kumar, K. Yadav, L. J. Li, Y. T. Chen, *ACS Appl Mater Interfaces* **2015**, *7*, 23328.

[53] L. Yang, W. Zhou, D. Hou, K. Zhou, G. Li, Z. Tang, L. Li, S. Chen, *Nanoscale* **2015**, *7*, 5203.

[54] Q. Qu, J. H. Zhang, J. Wang, Q. Y. Li, C. W. Xu, X. Lu, *Sci. Rep.* **2017**, *7*, 41542.

[55] D. Y. Wang, M. Gong, H. L. Chou, C. J. Pan, H. A. Chen, Y. Wu, M. C. Lin, M. Guan, J. Yang, C. W. Chen, Y. L. Wang, B. J. Hwang, C. C. Chen, H. Dai, *J. Am. Chem. Soc.* **2015**, *137*, 1587.

[56] X. Zou, Y. Liu, G. D. Li, Y. Wu, D. P. Liu, W. Li, H. W. Li, D. Wang, Y. Zhang, X. Zou, *Adv. Mater.* **2017**, *29*, 1700404.

[57] S. Yin, W. Tu, Y. Sheng, Y. Du, M. Kraft, A. Borgna, R. Xu, *Adv. Mater.* **2018**, *30*, 1705106.

[58] X. Zhou, Y. Liu, H. Ju, B. Pan, J. Zhu, T. Ding, C. Wang, Q. Yang, *Chem. Mater.* **2016**, *28*, 1838.

[59]F. Wang, P. He, Y. Li, T. A. Shifa, Y. Deng, K. Liu, Q. Wang, F. Wang, Y. Wen, Z. Wang, X. Zhan, L. Sun, J. He, *Adv. Funct. Mater.* **2017**, *27*, 1605802.

[60]L. Chen, J. Zhang, X. Ren, R. Ge, W. Teng, X. Sun, X. Li, *Nanoscale* **2017**, *9*, 16632.

[61]R. Subbaraman, D. Tripkovic, D. Strmcnik, K.-C. Chang, M. Uchimura, A. P. Paulikas, V. Stamenkovic, N. M. Markovic, *Science* **2011**, *334*, 1256.

[62]N. Danilovic, R. Subbaraman, D. Strmcnik, K. C. Chang, A. P. Paulikas, V. R. Stamenkovic, N. M. Markovic, *Angew. Chem. Int. Ed. Engl.* **2012**, *51*, 12495.

[63]W. Zhou, D. Hou, Y. Sang, S. Yao, J. Zhou, G. Li, L. Li, H. Liu, S. Chen, *J. Mater. Chem. A* **2014**, *2*, 11358.

[64]B. Conway, B. Tilak, *Electrochim. Acta* **2002**, *47*, 3571.

[65]A. J. Bard, L. R. Faulkner, J. Leddy, C. G. Zoski, *Electrochemical methods: fundamentals and applications*, wiley New York, **1980**.

[66]N. Danilovic, R. Subbaraman, D. Strmcnik, V. R. Stamenkovic, N. M. Markovic, *J. Serb. Chem. Soc.* **2013**, *78*, 2007.

[67]H. Lehmann, X. Fuentes-Arderiu, L. Bertello, *Pure Appl. Chem.* **1996**, *68*, 957.

[68]P. Quaino, F. Juarez, E. Santos, W. Schmickler, *Beilstein J Nanotechnol* **2014**, *5*, 846.

[69]R. Parsons, *Trans. Faraday Soc.* **1958**, *54*, 1053.

[70]S. Trasatti, *J. Electroanal. Chem. Interfacial Electrochem.* **1972**, *39*, 163.

[71]J. K. Nørskov, T. Bligaard, A. Logadottir, J. Kitchin, J. G. Chen, S. Pandelov, U. Stimming, *J. Electrochem. Soc.* **2005**, *152*, J23.

[72]B. Hinnemann, P. G. Moses, J. Bonde, K. P. Jørgensen, J. H. Nielsen, S. Horch, I. Chorkendorff, J. K. Nørskov, *J. Am. Chem. Soc.* **2005**, *127*, 5308.

[73]T. F. Jaramillo, K. P. Jørgensen, J. Bonde, J. H. Nielsen, S. Horch, I. Chorkendorff, *Science* **2007**, *317*, 100.

[74]Y. Li, H. Wang, L. Xie, Y. Liang, G. Hong, H. Dai, *J. Am. Chem. Soc.* **2011**, *133*, 7296.

[75]L. Liao, J. Zhu, X. Bian, L. Zhu, M. D. Scanlon, H. H. Girault, B. Liu, *Adv. Funct. Mater.* **2013**, *23*, 5326.

[76]E. Skúlason, V. Tripkovic, M. E. Björketun, S. Gudmundsdottir, G. Karlberg, J. Rossmeisl, T. Bligaard, H. Jónsson, J. K. Nørskov, *J. Phys. Chem. C* **2010**, *114*, 18182.

[77]Z. W. Seh, J. Kibsgaard, C. F. Dickens, I. Chorkendorff, J. K. Norskov, T. F. Jaramillo, *Science* **2017**, *355*.

[78]T. Schmidt, P. Ross, N. Markovic, *J. Electroanal. Chem.* **2002**, *524*, 252.

[79]K. Xu, H. Ding, M. Zhang, M. Chen, Z. Hao, L. Zhang, C. Wu, Y. Xie, *Adv. Mater.* **2017**, *29*, 1606980.

[80]K. K. Ghuman, S. Yadav, C. V. Singh, *J. Phys. Chem. C* **2015**, *119*, 6518.

[81]J. Luo, J.-H. Im, M. T. Mayer, M. Schreier, M. K. Nazeeruddin, N.-G. Park, S. D. Tilley, H. J. Fan, M. Grätzel, *Science* **2014**, *345*, 1593.

[82]J. D. Benck, T. R. Hellstern, J. Kibsgaard, P. Chakthranont, T. F. Jaramillo, *ACS Catal.* **2014**, *4*, 3957.

[83]A. R. Kucernak, C. Zalitis, *J. Phys. Chem. C* **2016**, *120*, 10721.

[84]T. Shinagawa, A. T. Garcia-Esparza, K. Takanabe, *Sci. Rep.* **2015**, *5*, 13801.

[85]C. H. Hamann, A. Hamnett, W. Vielstich, Weinheim, *Electrochemistry, Second Completely Revised and Updated Edition*, Wiley-VCH, **2007**.

[86]C. Cao, *Principles of electrochemistry of corrosion*, Chem. Ind. Press, Peking, China

2008.

[87]J. M. Thomas, W. J. Thomas, *Principles and practice of heterogeneous catalysis*, John Wiley & Sons, **2014**.

[88]C. Costentin, S. Drouet, M. Robert, J. M. Saveant, *J. Am. Chem. Soc.* **2012**, *134*, 11235.

[89]H. Li, C. Tsai, A. L. Koh, L. Cai, A. W. Contryman, A. H. Fragapane, J. Zhao, H. S. Han, H. C. Manoharan, F. Abild-Pedersen, *Nat. Mater.* **2016**, *15*, 48.

[90]S. Shin, Z. Jin, D. H. Kwon, R. Bose, Y. S. Min, *Langmuir* **2015**, *31*, 1196.

[91]J. Kibsgaard, T. F. Jaramillo, F. Besenbacher, *Nat. Chem.* **2014**, *6*, 248.

[92]Y. Yan, X. Ge, Z. Liu, J. Y. Wang, J. M. Lee, X. Wang, *Nanoscale* **2013**, *5*, 7768.

[93]D. Mukherjee, P. M. Austeria, S. Sampath, *ACS Energy Lett.* **2016**, *1*, 367.

[94]J. Zhang, L. Zhao, A. Liu, X. Li, H. Wu, C. Lu, *Electrochim. Acta* **2015**, *182*, 652.

[95]M. Ledendecker, G. Clavel, M. Antonietti, M. Shalom, *Adv. Funct. Mater.* **2015**, *25*, 393.

[96]Z.-x. Cai, X.-h. Song, Y.-r. Wang, X. Chen, *ChemElectroChem* **2015**, *2*, 1665.

[97]J. Deng, P. Ren, D. Deng, L. Yu, F. Yang, X. Bao, *Energy Environ. Sci.* **2014**, *7*, 1919.

[98]J. Deng, P. Ren, D. Deng, X. Bao, *Angew. Chem. Int. Ed. Engl.* **2015**, *54*, 2100.

[99]H. Tang, K. Dou, C.-C. Kaun, Q. Kuang, S. Yang, *J. Mater. Chem. A* **2014**, *2*, 360.

[100] J. Yang, D. Voiry, S. J. Ahn, D. Kang, A. Y. Kim, M. Chhowalla, H. S. Shin, *Angew. Chem. Int. Ed. Engl.* **2013**, *52*, 13751.

[101] Y. Lei, S. Pakhira, K. Fujisawa, X. Wang, O. O. Iyiola, N. s. Perea López, A. Laura Elías, L. Pulickal Rajukumar, C. Zhou, B. Kabius, *ACS nano* **2017**, *11*, 5103.

[102] T. A. Shifa, F. Wang, Z. Cheng, X. Zhan, Z. Wang, K. Liu, M. Safdar, L. Sun, J. He, *Nanoscale* **2015**, *7*, 14760.

[103] Y. Lin, Y. Pan, J. Zhang, Y. Chen, K. Sun, Y. Liu, C. Liu, *Electrochim. Acta* **2016**, *222*, 246.

[104] D. J. Li, U. N. Maiti, J. Lim, D. S. Choi, W. J. Lee, Y. Oh, G. Y. Lee, S. O. Kim, *Nano Lett.* **2014**, *14*, 1228.

[105] Q. Gong, Y. Wang, Q. Hu, J. Zhou, R. Feng, P. N. Duchesne, P. Zhang, F. Chen, N. Han, Y. Li, *Nat. Commun* **2016**, *7*, 13216.

[106] S. Peng, L. Li, X. Han, W. Sun, M. Srinivasan, S. G. Mhaisalkar, F. Cheng, Q. Yan, J. Chen, S. Ramakrishna, *Angew. Chem.* **2014**, *126*, 12802.

[107] P. Cao, J. Peng, J. Li, M. Zhai, *J. Power Sources* **2017**, *347*, 210.

[108] I. H. Kwak, H. S. Im, D. M. Jang, Y. W. Kim, K. Park, Y. R. Lim, E. H. Cha, J. Park, *ACS Appl Mater Interfaces* **2016**, *8*, 5327.

[109] D. Kong, J. J. Cha, H. Wang, H. R. Lee, Y. Cui, *Energy Environ. Sci.* **2013**, *6*, 3553.

[110] S. Xu, D. Li, P. Wu, *Adv. Funct. Mater.* **2015**, *25*, 1127.

[111] Q. Lu, Y. Yu, Q. Ma, B. Chen, H. Zhang, *Adv. Mater.* **2016**, *28*, 1917.

[112] H. Ren, Z.-H. Huang, Z. Yang, S. Tang, F. Kang, R. Lv, *J. Energy Chem.* **2017**, *26*, 1217.

[113] Y. Guo, C. Shang, E. Wang, *J. Mater. Chem. A* **2017**, *5*, 2504.

[114] X. Zhou, X. Yang, M. N. Hedhili, H. Li, S. Min, J. Ming, K.-W. Huang, W. Zhang, L.-J. Li, *Nano Energy* **2017**, *32*, 470.

[115] M. Wang, P. Ju, W. Li, Y. Zhao, X. Han, *Dalton Trans.* **2017**, *46*, 483.

[116] C. H. Mu, H. X. Qi, Y. Q. Song, Z. P. Liu, L. X. Ji, J. G. Deng, Y. B. Liao, F. Scarpa, *RSC Adv.* **2016**, *6*, 23.

[117] M. Wu, Y. Huang, X. Cheng, X. Geng, Q. Tang, Y. You, Y. Yu, R. Zhou, J. Xu, *Adv. Mater. Interfaces* **2017**, *4*, 1700948.

[118] Y.-R. Liu, W.-H. Hu, X. Li, B. Dong, X. Shang, G.-Q. Han, Y.-M. Chai, Y.-Q. Liu, C.-G. Liu, *Appl. Surf. Sci.* **2016**, *384*, 51.

[119] Y.-R. Liu, X. Shang, W.-K. Gao, B. Dong, J.-Q. Chi, X. Li, K.-L. Yan, Y.-M. Chai, Y.-Q. Liu, C.-G. Liu, *Appl. Surf. Sci.* **2017**, *412*, 138.

[120] J. Huang, D. Hou, Y. Zhou, W. Zhou, G. Li, Z. Tang, L. Li, S. Chen, *J. Mater. Chem. A* **2015**, *3*, 22886.

[121] P. Liu, J. A. Rodriguez, *J. Am. Chem. Soc.* **2005**, *127*, 14871.

[122] C. Wang, T. Ding, Y. Sun, X. Zhou, Y. Liu, Q. Yang, *Nanoscale* **2015**, *7*, 19241.

[123] X. Zhu, M. Liu, Y. Liu, R. Chen, Z. Nie, J. Li, S. Yao, *J. Mater. Chem. A* **2016**, *4*, 8974.

[124] Y. Pan, Y. Liu, Y. Lin, C. Liu, *ACS Appl. Mater. Interfaces* **2016**, *8*, 13890.

[125] M. Liu, L. Yang, T. Liu, Y. Tang, S. Luo, C. Liu, Y. Zeng, *J. Mater. Chem. A* **2017**, *5*, 8608.

[126] X. Wang, Y. V. Kolen'ko, X. Q. Bao, K. Kovnir, L. Liu, *Angew. Chem. Int. Ed.* **2015**, *54*, 8188.

[127] W. Tang, J. Wang, L. Guo, X. Teng, T. J. Meyer, Z. Chen, *ACS Appl. Mater. Interfaces* **2017**, *9*, 41347.

[128] Y.-R. Liu, W.-H. Hu, X. Li, B. Dong, X. Shang, G.-Q. Han, Y.-M. Chai, Y.-Q. Liu, C.-G. Liu, *Appl. Surf. Sci.* **2016**, *383*, 276.

[129] T. Wang, L. Wu, X. Xu, Y. Sun, Y. Wang, W. Zhong, Y. Du, *Sci. Rep.* **2017**, *7*, 11891.

[130] J. Jin, Y. Zhu, Y. Liu, Y. Li, W. Peng, G. Zhang, F. Zhang, X. Fan, *Int. J. Hydrogen Energy* **2017**, *42*, 3947.

[131] Y. Pan, Y. Lin, Y. Liu, C. Liu, *Catal. Sci. Technol.* **2016**, *6*, 1611.

[132] Y. N. Regmi, A. Roy, L. A. King, D. A. Cullen, H. M. Meyer, G. A. Goenaga, T. A. Zawodzinski, N. Labbé, S. C. Chmely, *Chem. Mater.* **2017**, *29*, 9369.

[133] E. S. Stoyanov, I. V. Stoyanova, C. A. Reed, *J. Am. Chem. Soc.* **2010**, *132*, 1484.

[134] J.-X. Feng, S.-Y. Tong, Y.-X. Tong, G.-R. Li, *J. Am. Chem. Soc.* **2018**, *140*, 5118.

[135] Z. Chen, D. Cummins, B. N. Reinecke, E. Clark, M. K. Sunkara, T. F. Jaramillo, *Nano Lett.* **2011**, *11*, 4168.

[136] X. Zhang, P. Ding, Y. Sun, Y. Wang, Y. Wu, J. Guo, *J. Alloys Compd.* **2017**, *715*, 53.

[137] C.-L. Wu, P.-C. Huang, S. Brahma, J.-L. Huang, S.-C. Wang, *Ceram. Int.* **2017**, *43*, S621.

[138] B. Jin, X. Zhou, L. Huang, M. Lickleder, M. Yang, P. Schmuki, *Angew. Chem. Int. Ed. Engl.* **2016**, *55*, 12252.

[139] Y. Huang, Y.-E. Miao, L. Zhang, W. W. Tjiu, J. Pan, T. Liu, *Nanoscale* **2014**, *6*, 10673.

[140] E. Pu, D. Liu, P. Ren, W. Zhou, D. Tang, B. Xiang, Y. Wang, J. Miao, *AIP Advances* **2017**, *7*, 025015.

[141] Q. Xie, X. Zheng, D. Wu, X. Chen, J. Shi, X. Han, X. Zhang, G. Peng, Y. Gao, H. Huang, *Appl. Phys. Lett.* **2017**, *111*, 093505.

[142] B. Galindo, S. G. Alcolea, J. Gómez, A. Navas, A. O. Murguialday, M. P. Fernandez, R. Puelles, presented at IOP Conference Series: Materials Science and Engineering **2014**.

[143] M. Opitz, D. Go, P. Lott, S. Müller, J. Stollenwerk, A. J. Kuehne, B. Roling, *J. Appl. Phys.* **2017**, *122*, 105104.

[144] E. Kemppainen, A. Bodin, B. Sebok, T. Pedersen, B. Seger, B. Mei, D. Bae, P. C. K. Vesborg, J. Halme, O. Hansen, *Energy Environ. Sci.* **2015**, *8*, 2991.

[145] S. Anantharaj, P. E. Karthik, B. Subramanian, S. Kundu, *ACS Catalysis* **2016**, *6*, 4660.

[146] Y. Cheng, S. Lu, F. Liao, L. Liu, Y. Li, M. Shao, *Adv. Funct. Mater.* **2017**, 1700359.

[147] M. Basu, R. Nazir, C. Mahala, P. Fageria, S. Chaudhary, S. Gangopadhyay, S. Pande, *Langmuir* **2017**, *33*, 3178.

[148] X. Huang, Z. Zeng, S. Bao, M. Wang, X. Qi, Z. Fan, H. Zhang, *Nat. Commun* **2013**, *4*, 1444.

[149] C. Wang, F. Hu, H. Yang, Y. Zhang, H. Lu, Q. Wang, *Nano Research* **2017**, *10*, 238.

[150] T. G. Kelly, S. T. Hunt, D. V. Esposito, J. G. Chen, *Int. J. Hydrogen Energy* **2013**, *38*, 5638.

[151] M. Basu, R. Nazir, P. Fageria, S. Pande, *Sci. Rep.* **2016**, *6*, 34738.

[152] J. Kim, S. Byun, A. J. Smith, J. Yu, J. Huang, *J. Phys. Chem. Lett.* **2013**, *4*, 1227.

[153] Y. Luo, D. Huang, M. Li, X. Xiao, W. Shi, M. Wang, J. Su, Y. Shen, *Electrochim. Acta* **2016**, *219*, 187.

[154] W.-F. Chen, J. T. Muckerman, E. Fujita, *Chem. Commun.* **2013**, *49*, 8896.

[155] L. Liao, S. Wang, J. Xiao, X. Bian, Y. Zhang, M. D. Scanlon, X. Hu, Y. Tang, B. Liu, H. H. Girault, *Energy Environ. Sci.* **2014**, *7*, 387.

[156] J. Houston, G. Laramore, R. L. Park, *Science* **1974**, *185*, 258.

[157] L. Bennett, J. Cuthill, A. McAlister, N. Erickson, R. Watson, *Science* **1974**, *184*, 563.

[158] L. Wang, Y. Li, M. Xia, Z. Li, Z. Chen, Z. Ma, X. Qin, G. Shao, *J. Power Sources* **2017**, *347*, 220.

[159] F. Harnisch, U. Schröder, M. Quaas, F. Scholz, *Appl. Catal., B* **2009**, *87*, 63.

[160] Y. Liu, G.-D. Li, L. Yuan, L. Ge, H. Ding, D. Wang, X. Zou, *Nanoscale* **2015**, *7*, 3130.

[161] J. Su, Y. Yang, G. Xia, J. Chen, P. Jiang, Q. Chen, *Nat. Commun.* **2017**, *8*, 14969.

[162] H. Fei, Y. Yang, Z. Peng, G. Ruan, Q. Zhong, L. Li, E. L. Samuel, J. M. Tour, *ACS Appl. Mater. Interfaces* **2015**, *7*, 8083.

[163] D. Zhou, L. He, W. Zhu, X. Hou, K. Wang, G. Du, C. Zheng, X. Sun, A. M. Asiri, *J. Mater. Chem. A* **2016**, *4*, 10114.

[164] T. Kokabu, S. Inoue, Y. Matsumura, *AIP Advances* **2016**, *6*, 115212.

[165] G. Birkett, D. Do, *J. Phys. Chem. C* **2007**, *111*, 5735.

[166] J. Ma, A. Michaelides, D. Alfe, L. Schimka, G. Kresse, E. Wang, *Phys. Rev. B* **2011**, *84*, 033402.

[167] X. Yu, J. Zhao, L.-R. Zheng, Y. Tong, M. Zhang, G. Xu, C. Li, J. Ma, G. Shi, *ACS Energy Lett.* **2017**, 237.

[168] B. Zhang, J. Liu, J. Wang, Y. Ruan, X. Ji, K. Xu, C. Chen, H. Wan, L. Miao, J. Jiang, *Nano Energy* **2017**, *37*, 74.

[169] J. Hu, C. Zhang, L. Jiang, H. Lin, Y. An, D. Zhou, M. K. Leung, S. Yang, *Joule* **2017**, *1*, 383.

[170] X. Zhang, Y. Liang, *Adv. Sci.* **2018**, *5*, 1700644.

[171] S.-Q. Liu, H.-R. Wen, G. Ying, Y.-W. Zhu, X.-Z. Fu, R. Sun, C.-P. Wong, *Nano Energy* **2018**, *44*, 7.

[172] M. Gao, L. Chen, Z. Zhang, X. Sun, S. Zhang, *J. Mater. Chem. A* **2018**, *6*, 833.

[173] X. Zhang, S. Zhu, L. Xia, C. Si, F. Qu, F. Qu, *Chem Commun (Camb)* **2018**, *54*, 1201.

[174] L. Xie, X. Ren, Q. Liu, G. Cui, R. Ge, A. M. Asiri, X. Sun, Q. Zhang, L. Chen, *J. Mater. Chem. A* **2018**.

[175] Z. Xing, C. Han, D. Wang, Q. Li, X. Yang, *ACS Catal.* **2017**, *7*, 7131.

[176] H. Yin, S. Zhao, K. Zhao, A. Muqsit, H. Tang, L. Chang, H. Zhao, Y. Gao, Z. Tang, *Nat. Commun.* **2015**, *6*, 6430.

[177] M. A. Henderson, *Surf. Sci. Rep.* **2002**, *46*, 1.

[178] A. Hodgson, S. Haq, *Surf. Sci. Rep.* **2009**, *64*, 381.

[179] H. Xu, R. Q. Zhang, A. M. Ng, A. B. Djurišić, H. T. Chan, W. K. Chan, S. Tong, *J. Phys. Chem. C* **2011**, *115*, 19710.

[180] M. Gong, W. Zhou, M. C. Tsai, J. Zhou, M. Guan, M. C. Lin, B. Zhang, Y. Hu, D. Y. Wang, J. Yang, S. J. Pennycook, B. J. Hwang, H. Dai, *Nat. Commun.* **2014**, *5*, 4695.

[181] Z. Weng, W. Liu, L.-C. Yin, R. Fang, M. Li, E. I. Altman, Q. Fan, F. Li, H.-M. Cheng, H. Wang, *Nano Lett.* **2015**, *15*, 7704.

[182] R. Zhang, X. Ren, S. Hao, R. Ge, Z. Liu, A. M. Asiri, L. Chen, Q. Zhang, X. Sun, *J. Mater. Chem. A* **2018**, *6*.

[183] Z. Wang, H. Du, Z. Liu, H. Wang, A. M. Asiri, X. Sun, *Nanoscale* **2018**, *10*, 2213.

[184] C. Wang, B. Tian, M. Wu, J. Wang, *ACS Appl. Mater. Interfaces* **2017**, *9*, 7084.

[185] Z. Wang, Z. Liu, G. Du, A. M. Asiri, L. Wang, X. Li, H. Wang, X. Sun, L. Chen, Q. Zhang, *Chem. Commun.* **2018**, *54*, 810.

[186] J. X. Feng, H. Xu, Y. T. Dong, X. F. Lu, Y. X. Tong, G. R. Li, *Angew. Chem.* **2017**, *129*, 3006.

[187] M. Janjua, R. Le Roy, *Int. J. Hydrogen Energy* **1985**, *10*, 11.

[188] M. Gong, D.-Y. Wang, C.-C. Chen, B.-J. Hwang, H. Dai, *Nano Research* **2016**, *9*, 28.

[189] M. Devanathan, M. Selvaratnam, *Trans. Faraday Soc.* **1960**, *56*, 1820.

[190] N. Krstajić, M. Popović, B. Grgur, M. Vojnović, D. Šepa, *J. Electroanal. Chem.* **2001**, *512*, 16.

[191] C. González-Buch, I. Herraiz-Cardona, E. M. Ortega, S. Mestre, V. Pérez-Herranz, *Int. J. Hydrogen Energy* **2016**, *41*, 764.

[192] C. Zhang, S. Liu, Z. Mao, X. Liang, B. Chen, *J. Mater. Chem. A* **2017**, *5*, 16646.

[193] S. Fiameni, I. Herraiz-Cardona, M. Musiani, V. Pérez-Herranz, L. Vázquez-Gómez, E. Verlato, *Int. J. Hydrogen Energy* **2012**, *37*, 10507.

[194] C. He, G. Wang, J. Parrondo, S. Sankarasubramanian, V. Ramani, *J. Electrochem. Soc.* **2017**, *164*, F1234.

[195] T. An, Y. Wang, J. Tang, W. Wei, X. Cui, A. M. Alenizi, L. Zhang, G. Zheng, *J. Mater. Chem. A* **2016**, *4*, 13439.

[196] H. Liu, X. Ma, Y. Rao, Y. Liu, J. Liu, L. Wang, M. Wu, *ACS Appl. Mater. Interfaces* **2018**, *10*, 10890.

[197] M. Wu, S. Wang, J. Wang, *Electrochim. Acta* **2017**, *258*, 669.

[198] C. Wang, P. Zhang, J. Lei, W. Dong, J. Wang, *Electrochim. Acta* **2017**, *246*, 712.

[199] P. Chen, K. Xu, S. Tao, T. Zhou, Y. Tong, H. Ding, L. Zhang, W. Chu, C. Wu, Y. Xie, *Adv. Mater.* **2016**, *28*, 7527.

[200] G. Zhao, P. Li, K. Rui, Y. Chen, S. X. Dou, W. Sun, *Chem. Eur. J* **2018**, DOI: 10.1002/chem.201801693.

[201] Y.-Y. Chen, Y. Zhang, W.-J. Jiang, X. Zhang, Z. Dai, L.-J. Wan, J.-S. Hu, *ACS nano* **2016**, *10*, 8851.

[202] G.-Q. Han, X. Li, J. Xue, B. Dong, X. Shang, W.-H. Hu, Y.-R. Liu, J.-Q. Chi, K.-L. Yan, Y.-M. Chai, C.-G. Liu, *Int. J. Hydrogen Energy* **2017**, *42*, 2952.

[203] Y. Zhao, K. Kamiya, K. Hashimoto, S. Nakanishi, *Angew. Chem. Int. Ed.* **2013**, *52*, 13638.

[204] Z. Xing, D. Wang, Q. Li, A. M. Asiri, X. Sun, *Electrochim. Acta* **2016**, *210*, 729.

[205] R. Kumar, R. Rai, S. Gautam, A. De Sarkar, N. Tiwari, S. N. Jha, D. Bhattacharyya, A. K. Ganguli, V. Bagchi, *J. Mater. Chem. A* **2017**, *5*, 7764.

[206] Z. Deng, J. Wang, Y. Nie, Z. Wei, *J. Power Sources* **2017**, *352*, 26.

[207] H. Ren, W. Xu, S. Zhu, Z. Cui, X. Yang, A. Inoue, *Electrochim. Acta* **2016**, *190*, 221.

[208] T. Li, K. Niu, M. Yang, N. K. Shrestha, Z. Gao, Y.-Y. Song, *J. Power Sources* **2017**, *356*, 89.

[209] X. Shang, J.-Q. Chi, S.-S. Lu, B. Dong, X. Li, Y.-R. Liu, K.-L. Yan, W.-K. Gao, Y.-M. Chai, C.-G. Liu, *Int. J. Hydrogen Energy* **2017**, *42*, 4165.

[210] D. Yoon, J. Lee, B. Seo, B. Kim, H. Baik, S. H. Joo, K. Lee, *Small* **2017**, *13*.

[211] A. C. Mtukula, X. Bo, L. Guo, *J. Alloys Compd.* **2017**, *692*, 614.

[212] X. Zheng, J. Xu, K. Yan, H. Wang, Z. Wang, S. Yang, *Chem. Mater.* **2014**, *26*, 2344.

[213] L. Zhu, H. Lin, Y. Li, F. Liao, Y. Lifshitz, M. Sheng, S.-T. Lee, M. Shao, *Nat. Commun.* **2016**, *7*, 12272.

[214] N. Bai, Q. Li, D. Mao, D. Li, H. Dong, *ACS Appl. Mater. Interfaces* **2016**, *8*, 29400.

[215] H. Liu, X. Ma, Y. Rao, Y. Liu, J. Liu, L. Wang, M. Wu, *ACS Appl. Mater. Interfaces* **2018**, *13*, 10890.

[216] L. Zhang, K. Xiong, S. Chen, L. Li, Z. Deng, Z. Wei, *J. Power Sources* **2015**, *274*, 114.

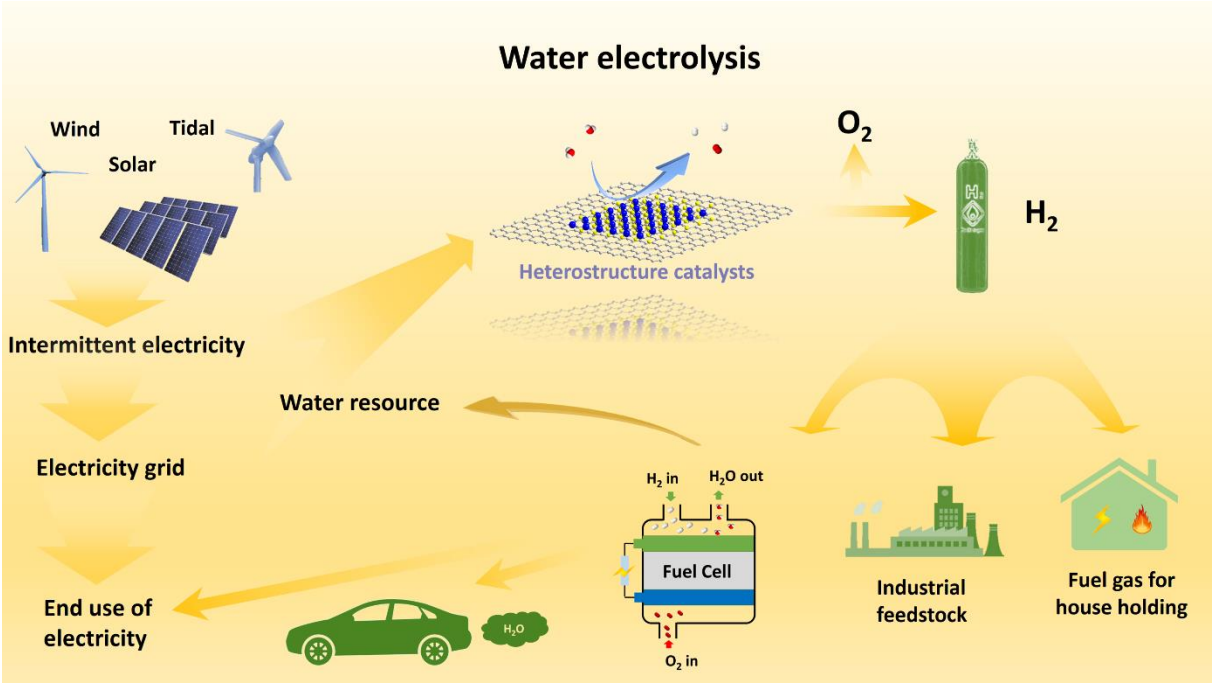

Figure 1. A sustainable pathway for the production and utilization of hydrogen energy.

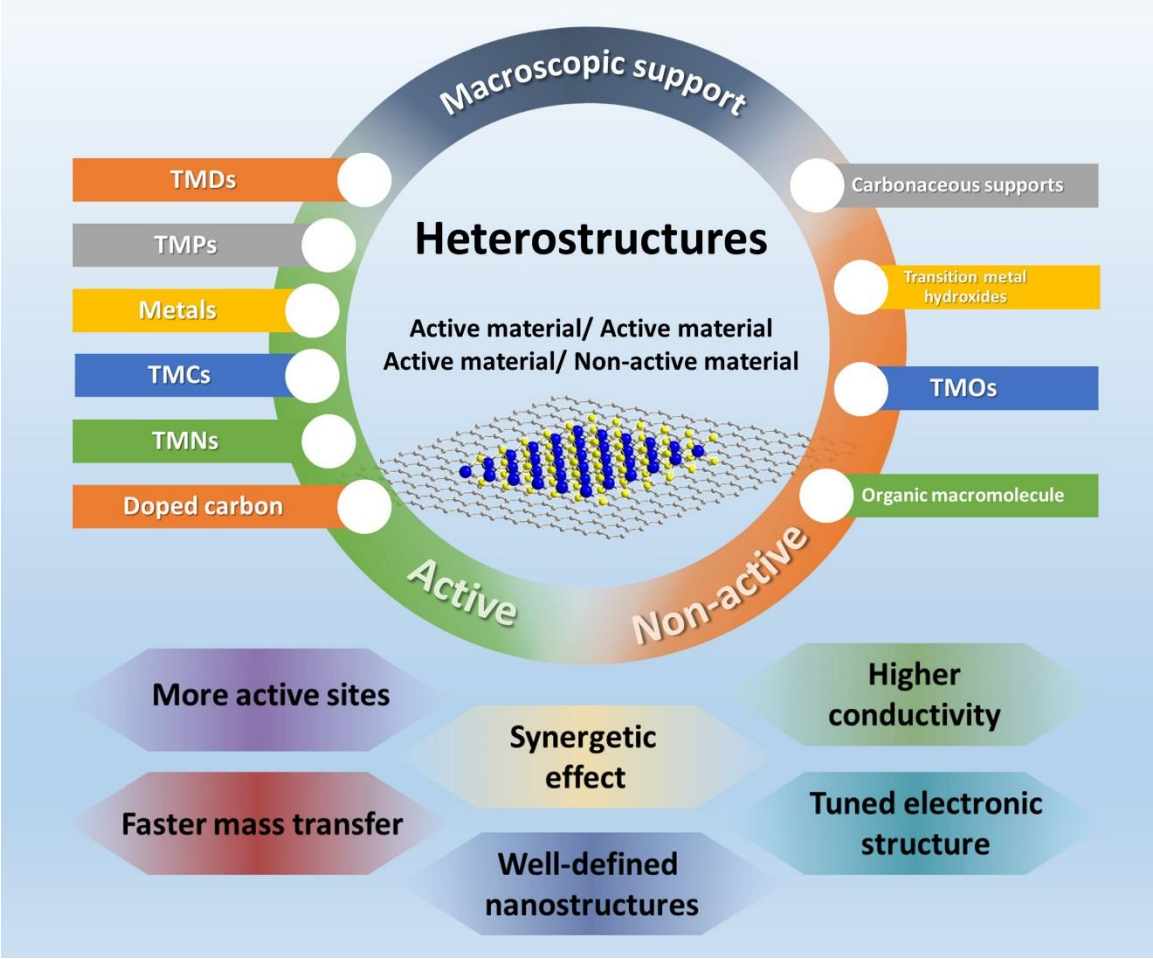

Figure 2. Heterostructured catalysts for HER and their superiorities for achieving enhanced catalytic activity.

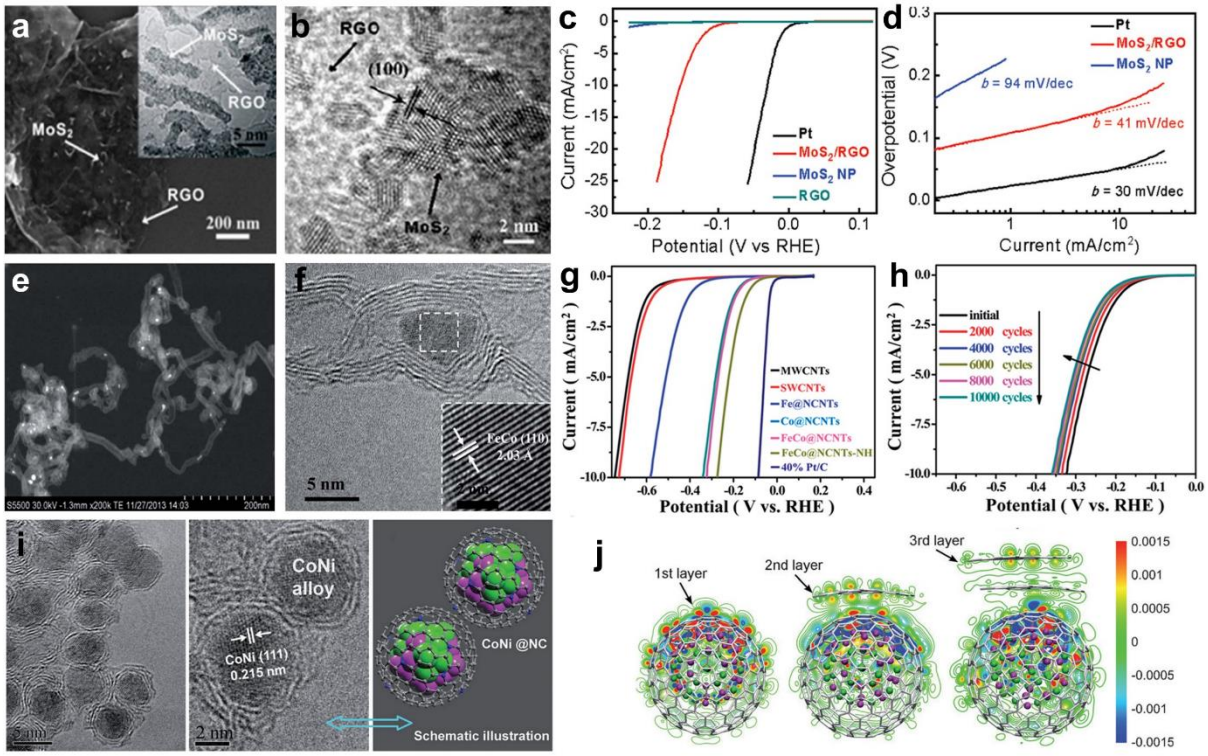

Figure 3. (a) SEM and TEM (inset) images of the MoS_2/RGO heterostructures. (b) HRTEM image showing nano-sized MoS_2 with highly exposed edges stacking on an RGO sheet. (c) LSV curves and (d) the corresponding Tafel plots obtained with several catalysts as indicated, electrolyte: 0.5 M H_2SO_4, catalyst loading: 0.28 mg cm^{-2}, sweep rate: 2 mV s^{-1}. Reproduced with permission.[74] Copyright 2011, American Chemical Society. (e) STEM image of FeCo@NCNTs. (f) HRTEM image of FeCo@NCNTs, the inset shows the (110) crystal plane of the FeCo nanoparticle. (g) LSV curves of various catalysts as indicated, electrolyte: 0.1 M H_2SO_4, catalyst loading: 0.28 mg cm^{-2}, sweep rate: 2 mV s^{-1}. (h) Durability measurement of FeCo@NCNTs: LSV curves recorded initially and after every 2000 CV sweeps between +0.77 and -0.18 V (vs. RHE) at 100 mV s^{-1}. Reproduced with permission.[97] Copyright 2014, The Royal Society of Chemistry. (i) HRTEM images of CoNi@NC showing the graphene shells and encapsulated metal nanoparticles, and the schematic illustration of the CoNi@NC structure. (j) The electron densities redistribution after the CoNi clusters have covered by one to three layers of graphene. The differential charge density is defined as the difference in the electron density with and without the CoNi cluster. The red and blue regions are regions of increased and decreased electron density, respectively. Reproduced with permission.[98] Copyright 2015, Wiley-VCH.

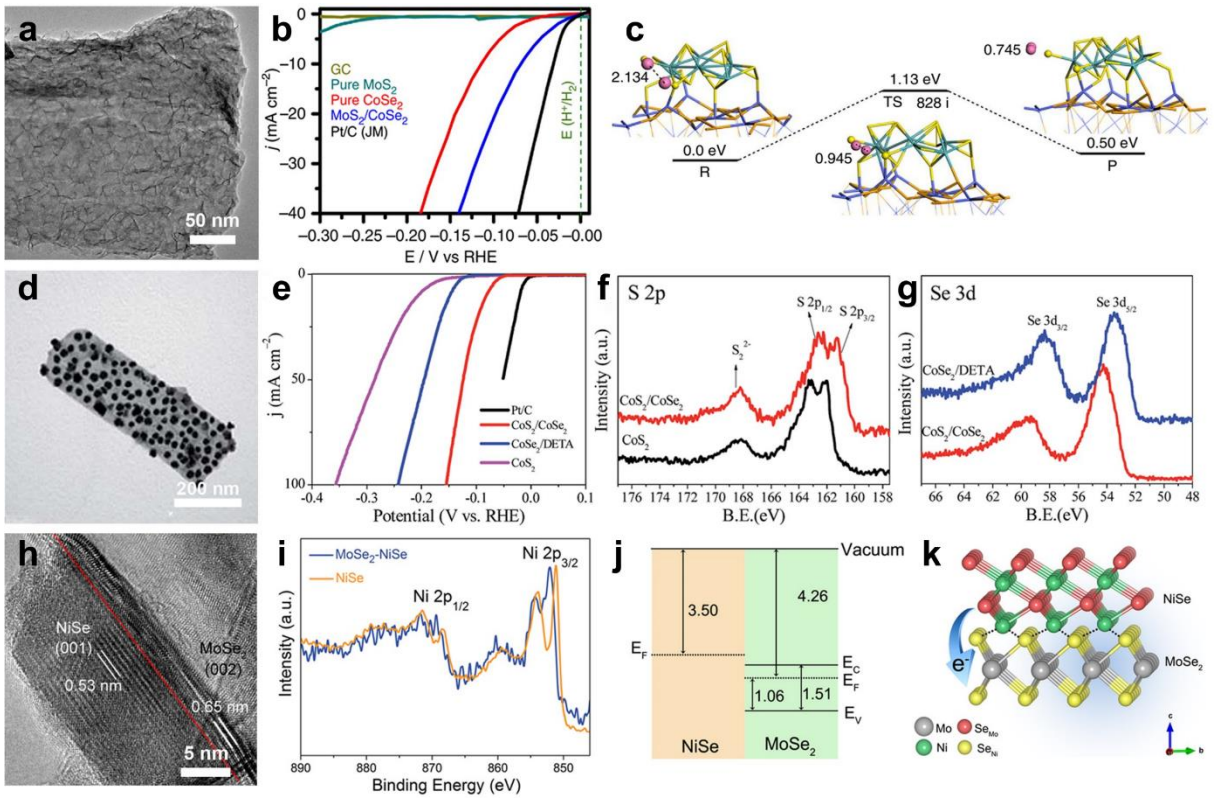

Figure 4. (a) TEM image of $MoS_2/CoSe_2$ heterostructures. (b) LSV curves for HER on various catalysts as indicated, electrolyte: 0.5 M H_2SO_4, catalyst loading: 0.28 mg cm^{-2}, sweep rate: 2 mV s^{-1}. (c) Reaction pathway of HER on $MoS_2/CoSe_2$ heterostructures based on the Volmer-Tafel route. Blue, orange, azure, yellow and pink indicate Co, Se, Mo, S and H atoms, respectively. Reproduced with permission.[49] Copyright 2015, Macmillan Publishers Limited. (d) TEM image of the $CoS_2/CoSe_2$ heterostructures. (e) LSV curves of various catalysts as indicated, electrolyte: 0.5 M H_2SO_4, catalyst loading 0.28 mg cm^{-2}, sweep rate: 5 mV s^{-1}. (f) S 2p and (g) Se 3d XPS spectra of different materials as indicated. Reproduced with permission.[113] Copyright 2017, The Royal Society of Chemistry. (h) Cross-sectional HRTEM image of the $MoSe_2$/NiSe heterostructure. (i) Ni 2p XPS spectra of the bare NiSe and the $MoSe_2$/NiSe heterostructure. (j) Schematic energy band diagrams of interfacial $MoSe_2$/NiSe deduced by the UPS data. (k) Schematic illustration of the $MoSe_2$/NiSe heterostructures and the electron transfer from the NiSe nanocrystallites to the $MoSe_2$ substrate in the hetero-interface. Reproduced with permission.[58] Copyright 2016, American Chemical Society.

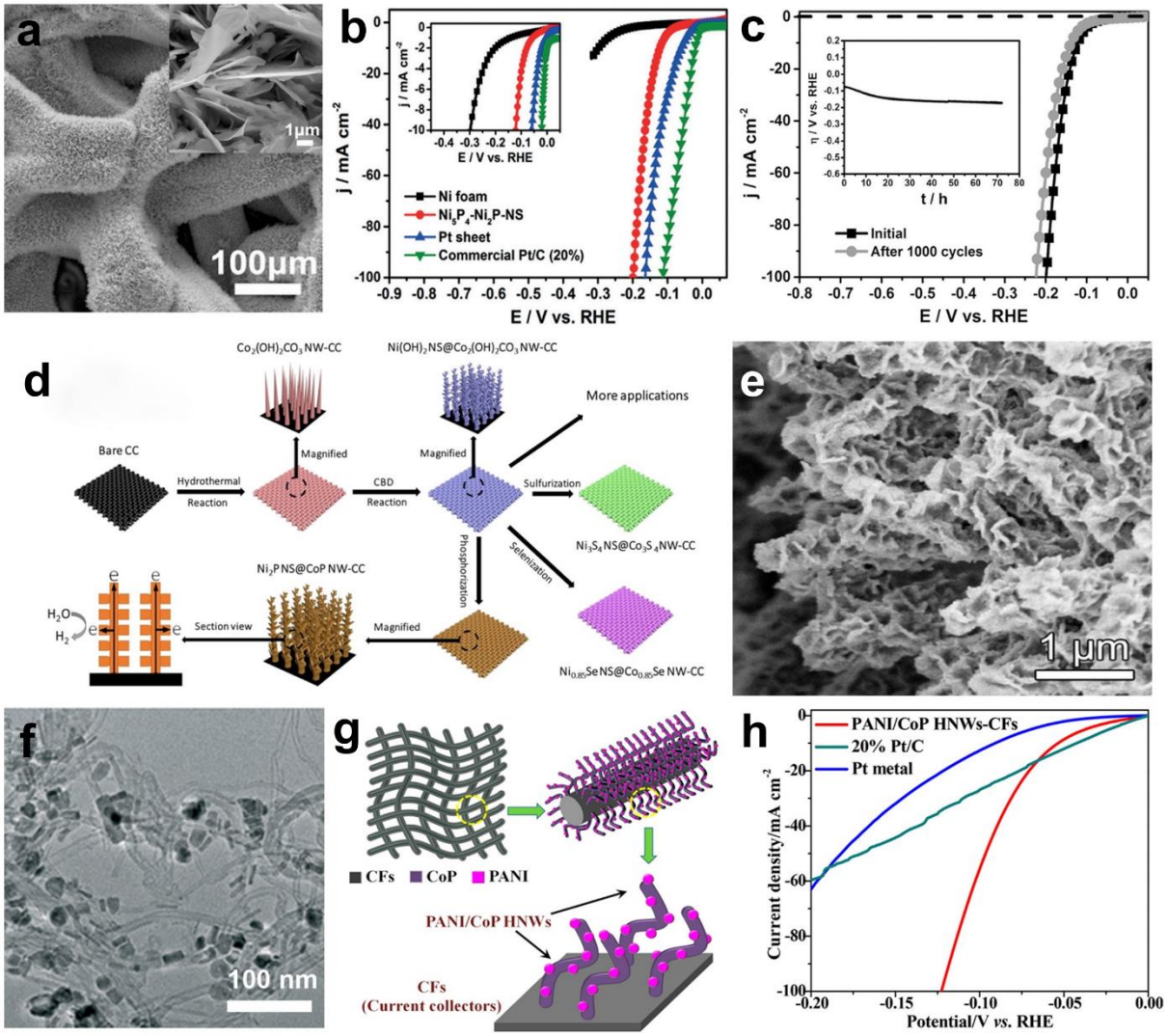

Figure 5. (a) SEM image of Ni_5P_4-Ni_2P-NS array cathode, the inset is a high-magnification SEM image. (b) LSV curves of various catalysts as indicated, electrolyte: 0.5 M H_2SO_4, sweep rate: 10 mV s^{-1}. (c) LSV curves of the Ni_5P_4-Ni_2P-NS array cathode measured before and after accelerated degradation test for 1000 continuous cycles, sweep rate: 10 mV s^{-1}. Inset: overpotential~t profile recorded at a constant cathodic current of 10 mA cm^{-2}. All measurements were performed in N_2-saturated 0.5 M H_2SO_4 solution at room temperature. Reproduced with permission.[126] Copyright 2015, Wiley-VCH. (d) Schematic diagram illustrating the procedure for preparing Ni_2P/CoP/CC electrode. (e) SEM image of the Ni_2P/CoP/CC electrode. Reproduced with permission.[127] Copyright 2017, American Chemical Society. (f) TEM image of the CoP/MoS_2-CNT heterostructure. Reproduced with permission.[131] Copyright 2016, The Royal Society of Chemistry. (g) Schematic illustration of the PANI/CoP HNWs-CFs heterostructures. (h) LSV curves of the PANI/CoP HNWs-CFs heterostructures (0.8 mg cm^{-2}), Pt metal (Pt loading: 4.5 mg cm^{-2}) and 20 wt% Pt/C (Pt loading: 0.012 mg cm^{-2}). Reproduced with permission.[134] Copyright 2018, American Chemical Society.

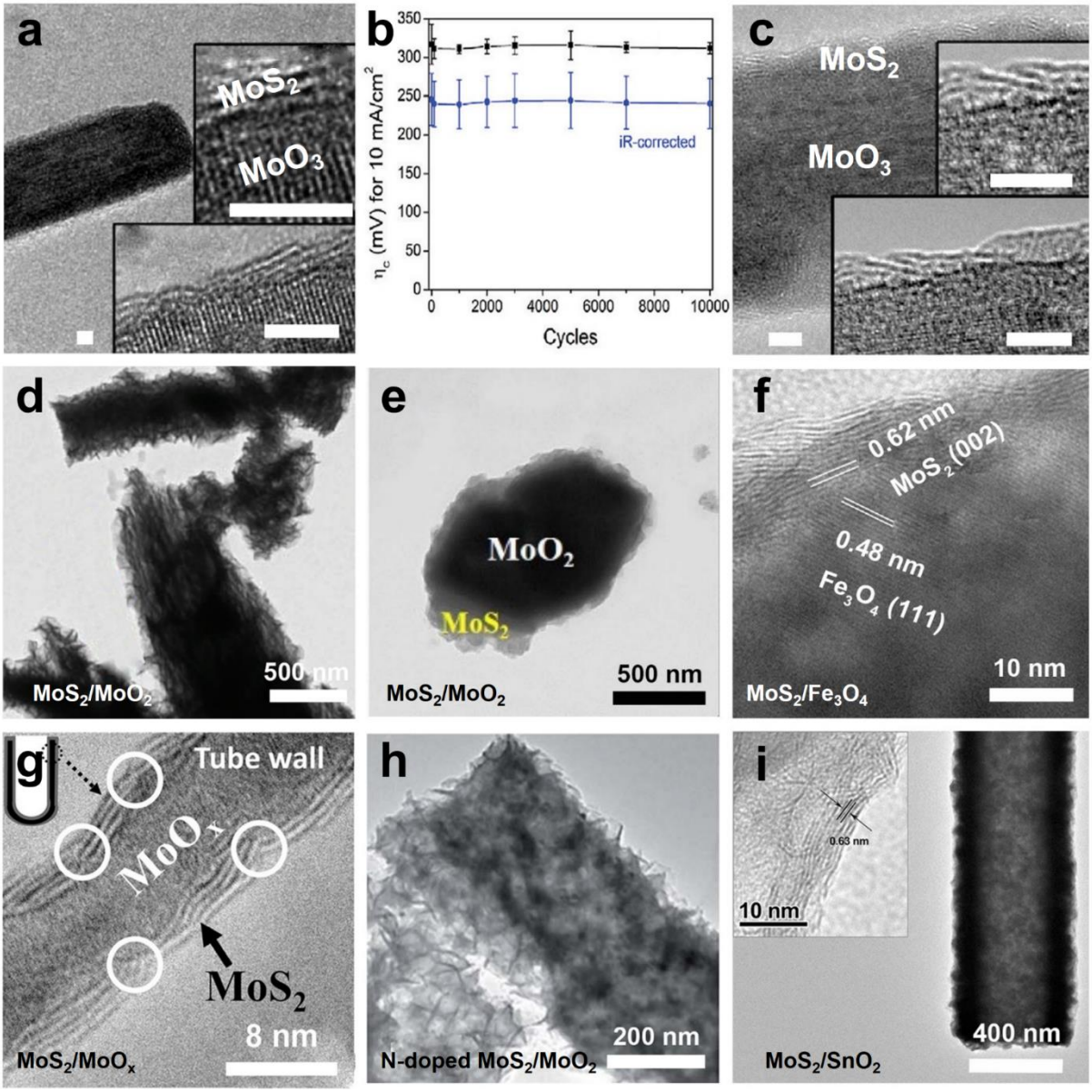

Figure 6. (a) TEM image of MoS_2/MoO_3 nanowires sulfidized at 200 °C, the inset HRTEM shows the lattice fringe of MoO_3 and MoS_2, scale bar: 5 nm. (b) The overpotential stability required to drive 10 mA cm^{-2} with iR correction (blue circles) and without iR correction (black squares). Data points are an average of 3 samples, while error bars represent a 95% confidence interval (two standard deviations). (c) TEM image of the MoS_2/MoO_3 nanowires after 10000 potential cycles. Reproduced with permission.[135] Copyright 2011, American Chemical Society. (d) TEM image of MoS_2/MoO_2 heterostructure. Reproduced with permission.[53] Copyright 2015, The Royal Society of Chemistry. (e) TEM image of MoS_2/MoO_2 heterostructure. Reproduced with permission.[137] Copyright 2017, Elsevier Ltd. (f) TEM image of MoS_2/Fe_3O_4 heterostructure. Reproduced with permission.[136] Copyright 2017, Elsevier Ltd. (g) TEM image of MoO_x/MoS_2 core–shell structure (annealed in H_2S at 500 °C for 2 min). Inset: position where this TEM image was taken from on the tube wall. The stacking misalignments of MoS_2 layers are marked in the white circles. Reproduced with permission.[138] Copyright 2016, Wiley-VCH. (h) TEM image of N-doped MoS_2/MoO_2. Reproduced with permission.[63] Copyright 2014, The Royal Society of Chemistry. (i) TEM image of MoS_2/SnO_2, the inset shows the HRTEM image of MoS_2 nanosheets. Reproduced

with permission.[139] Copyright 2014, The Royal Society of Chemistry.

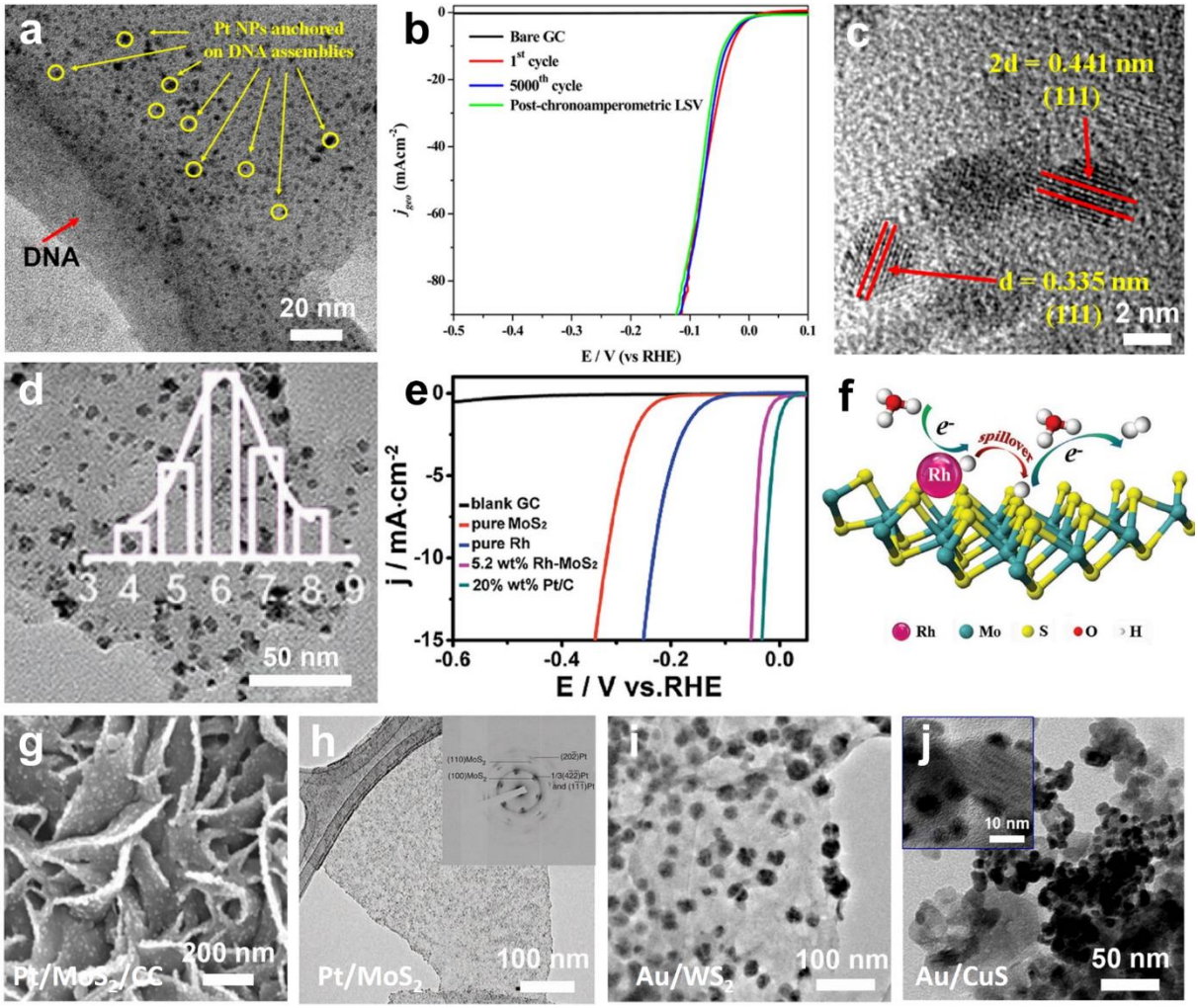

Figure 7. (a) HRTEM image of Pt/DNA molecular self-assemblies. (b) LSV curves of the Pt/DNA catalyst without binder at the first cycle and after 5000 cycles of accelerated degradation along with the post-chronoamperometric LSV and the LSV of bare GC, electrolyte: 0.5 M H_2SO_4, sweep rate: 2mV s^{-1}. (c) HRTEM image of Pt/DNA shows clear lattice fringes assigned to their respective planes in the Pt NPs after HER and aging studies. Reproduced with permission.[145] Copyright 2016, American Chemical Society. (d) TEM image of 5.2 wt% Rh-MoS_2, the inset shows the size distribution of Rh. (e) LSV curves of various catalysts as indicated, electrolyte: 0.5 M H_2SO_4, catalyst loading: 0.31 mg cm^{-2}, sweep rate: 5 mV s^{-1}. (f) The illustration for the feasible HER mechanism for the 5.2 wt% Rh-MoS_2 catalyst. Reproduced with permission.[146] Copyright 2017, Wiley-VCH. (g) SEM image of Pt/MoS_2/CC electrode. Reproduced with permission.[153] Copyright 2016, Elsevier Ltd. (h) TEM image of epitaxial Pt/MoS_2 heterostructure, the inset is the corresponding FFT patterns showing the epitaxial relationship. Reproduced with permission.[148] Copyright 2015, Macmillan Publishers Limited. (i) TEM image of Au nanoparticles on WS_2 sheet. Reproduced with permission.[152] Copyright 2013, American Chemical Society. (j) TEM image of CuS/Au heterostructures, the inset shows small Au particles on CuS plates. Reproduced with permission.[151] Copyright 2016, Springer Nature.

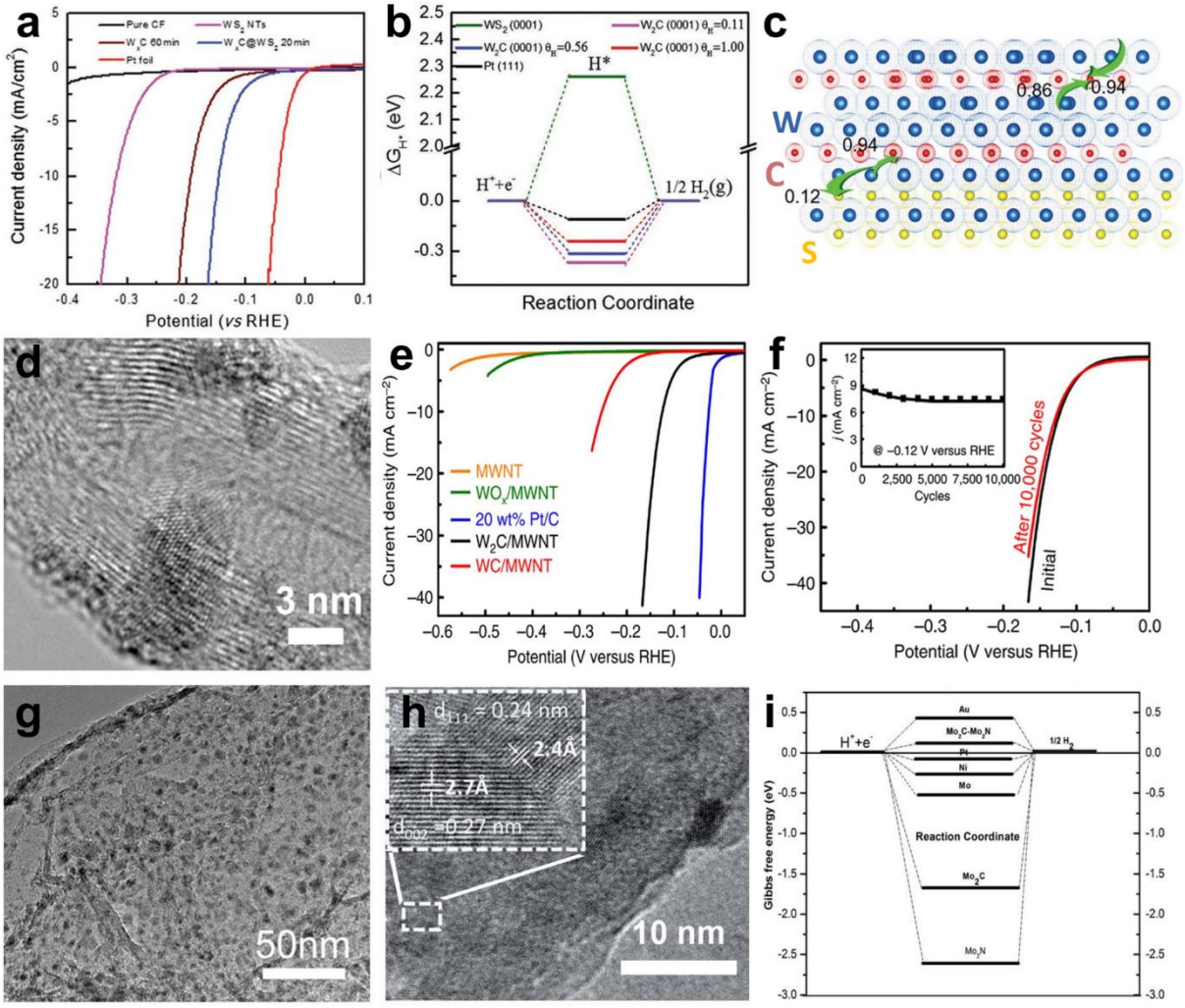

Figure 8. (a) LSV curves and corresponding Tafel plots for HER of various electrodes, electrolyte: 0.5 M H_2SO_4, catalyst loading: 0.3 mg cm^{-2}, sweep rate: 5 mV s^{-1}. (b) Free energy diagram of HER under different H* coverage (θ_H = 0.11, 0.56, and 1), as well as the comparison with Pt(111) and WS_2 terrace sites. (c) Charge redistribution in W_2C@WS_2 heterostructure. The arrows denote the electron transfer direction. Reproduced with permission.[59] Copyright 2017, Wiley-VCH. (d) HRTEM images of W_2C/MWNT. (e) LSV curves of various catalysts as indicated, electrolyte: 0.5 M H_2SO_4, catalyst loading: 0.56 mg cm^{-2}, sweep rate: 10 mV s^{-1}. (f) LSV curves of W_2C/MWNT before and after 10,000 potential cycles, sweep rate: 10 mV s^{-1}. The inset shows the change of HER cathodic current density at -120 mV vs. RHE with respect to the number of potential cycles. Reproduced with permission.[105] Copyright 2016, Springer Nature. (g) TEM images of P-WN/RGO. Reproduced with permission.[43] Copyright 2015, Wiley-VCH. (h) HRTEM of Mo_2N/Mo_2C heterostructures showing the interfaces of g-Mo_2N and b-Mo_2C nanocrystals. (i) The calculated free-energy diagram of the HER at the equilibrium potential on the surface of various catalysts as indicated. Reproduced with permission.[205] Copyright 2017, The Royal Society of Chemistry.

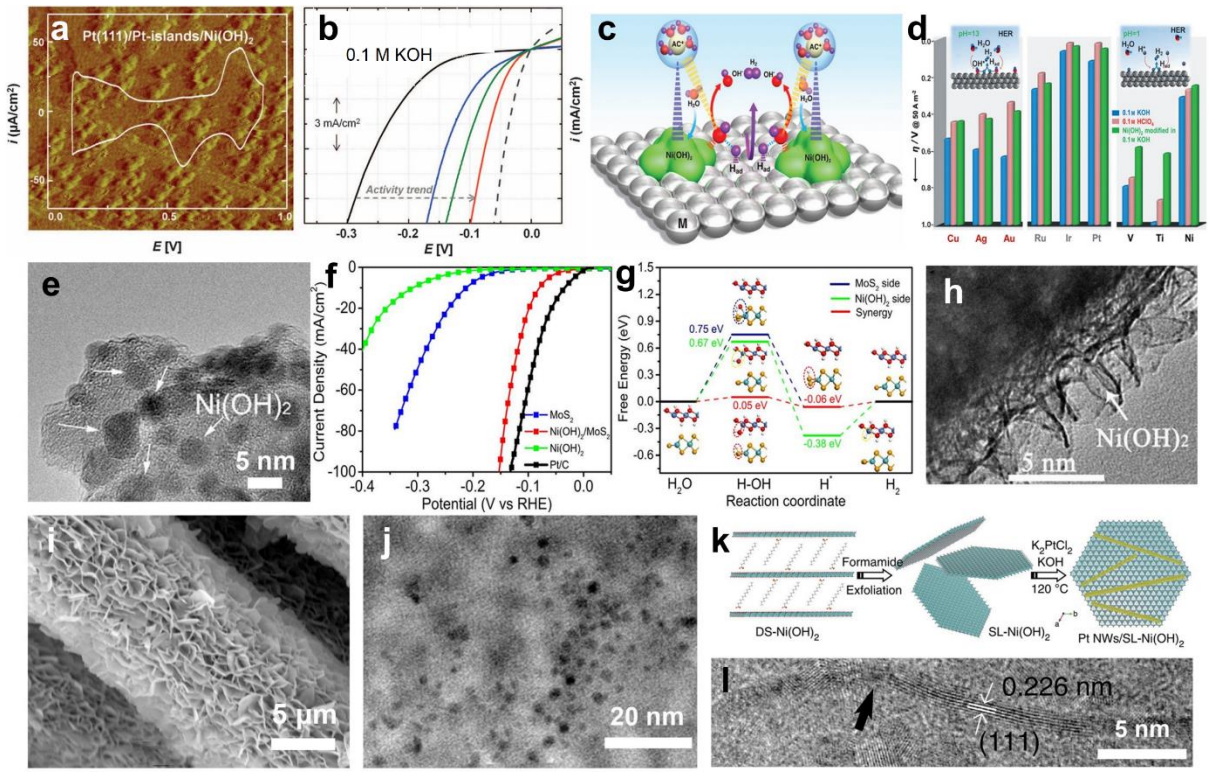

Figure 9. (a) STM image (60 × 60 nm^2) and CV trace of the $Ni(OH)_2$/Pt-islands/Pt(111) surface. Clusters of $Ni(OH)_2$ in the STM image appear ellipsoidal with particle sizes between 4 and 12 nm. (b) Comparison of HER activities with Pt(111) as the substrate, with the incremental HER activity sequence: the bare Pt(111) (black line), Pt(111)/$Ni(OH)_2$ (blue line), Pt(111)/$Ni(OH)_2$/Pt nanocluster (green line), Pt(111)/$Ni(OH)_2$/Pt nanocluster/10^{-3} M Li^+ (red line), and Pt(111) in 0.1 M $HClO_4$ (dashed line), electrolyte: 0.1 M KOH, sweep rate: 50 mV s^{-1}. (c) Schematic representation of the HER process on $Ni(OH)_2$/Pt electrode surface. Reproduced with permission.[61] Copyright 2011, AAAS. (d) Comparison between activities for the HER, expressed as overpotential required for a 5 mA cm^{-2} current density, in 0.1 M $HClO_4$ and 0.1 M KOH for both bare metal surfaces and $Ni(OH)_2$-modified surfaces. Reproduced with permission.[62] Copyright 2012, Wiley-VCH. (d) TEM image of the $Ni(OH)_2/MoS_2$ heterostructure. (f) LSV curves of various catalysts as indicated，electrolyte: 1 M KOH, sweep rate： 2 mV s^{-1}. (g) The corresponding free energy diagram for HER on the MoS_2 edge and $Ni(OH)_2/MoS_2$ interface. The surface structures of catalysts at different stages are shown in the inset. Reproduced with permission.[168] Copyright 2017, Elsevier Ltd. (h) TEM image of $Ni(OH)_2/CoS_2$ heterostructure, showing $Ni(OH)_2$ layers on the surface of CoS_2 nanowires. Reproduced with permission.[60] Copyright 2017, Royal Society of Chemistry. (i) SEM image of the Pt/$Co(OH)_2$/CC electrode. (j) TEM image of Pt/$Co(OH)_2$ heterostructure. Reproduced with permission.[175] Copyright 2017, American Chemical Society. (k) Scheme for synthesis of Pt NWs/SL-$Ni(OH)_2$. (l) TEM images of Pt NWs/SL-$Ni(OH)_2$. Reproduced with permission.[176] Copyright 2015, Springer Nature.

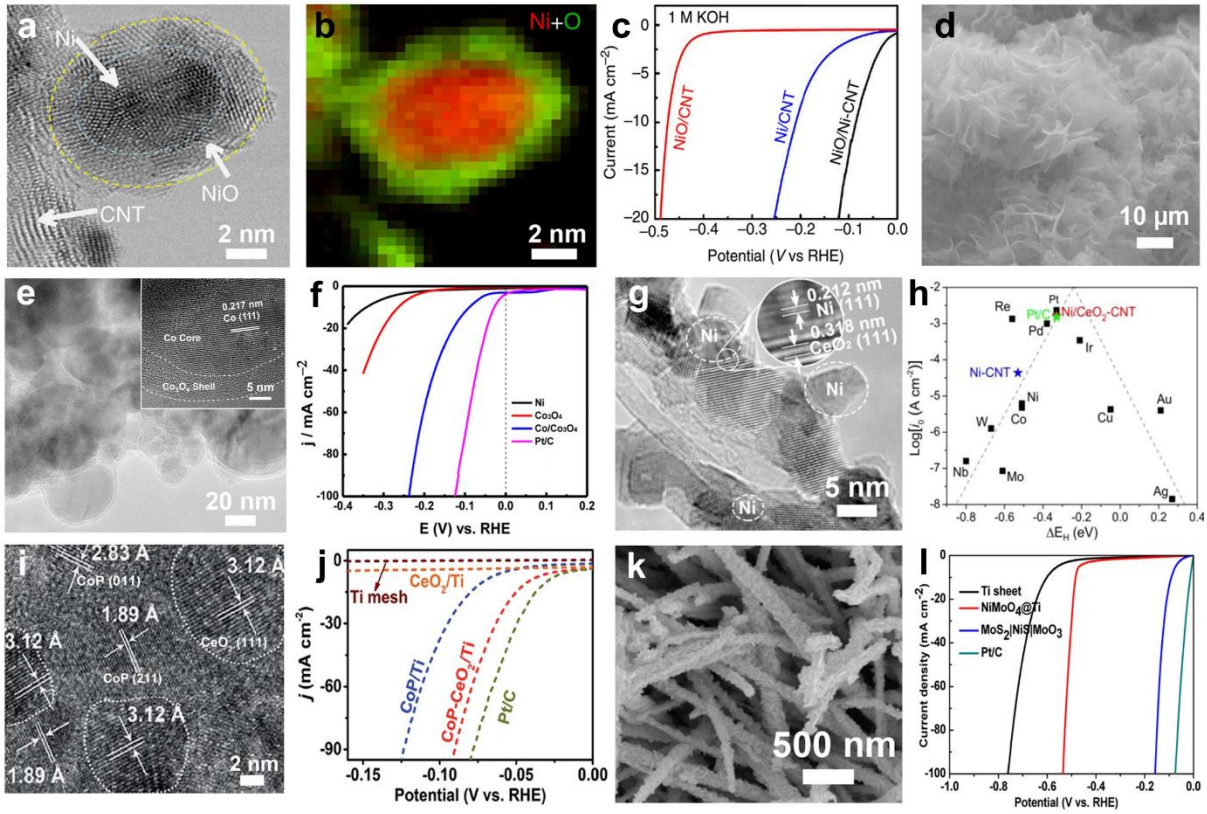

Figure 10. (a) HRTEM image of the NiO/Ni-CNT heterostructures. (b) The corresponding EDX mapping image of (a). (c) LSV curves of various catalysts as indicated, electrolyte: 1 M KOH, catalyst loading: 0.28 mg cm^{-2}, sweep rate 1 mV s^{-1}. Reproduced with permission.[180] Copyright 2015, Springer Nature. (d) SEM and (e) TEM images of Co/Co_3O_4 nanosheets, the inset shows the core-shell structure. (f) LSV curves of various catalysts as indicated, electrolyte: 1 M KOH, sweep rate: 2 mV s^{-1}. Reproduced with permission.[50] Copyright 2015, American Chemical Society. (g) HRTEM image of the Ni/CeO_2-CNT heterostructure. (h) The volcano plot of the experimentally measured exchange current density vs. the DFT calculated hydrogen binding energy. Reproduced with permission.[181] Copyright 2015, American Chemical Society. (i) HRTEM image of the CoP-CeO_2 nanosheet. (j) LSV curves of various catalysts as indicated, electrolyte: 1 M KOH, sweep rate: 2 mV s^{-1}. Reproduced with permission.[182] Copyright 2018, The Royal Society of Chemistry. (k) SEM image of the $MoS_2/NiS/MoO_3$ heterostructures. (l) LSV curves of various catalysts as indicated, electrolyte: 1 M KOH, sweep rate: 2 mV s^{-1}. Reproduced with permission.[184] Copyright 2011, American Chemical Society.

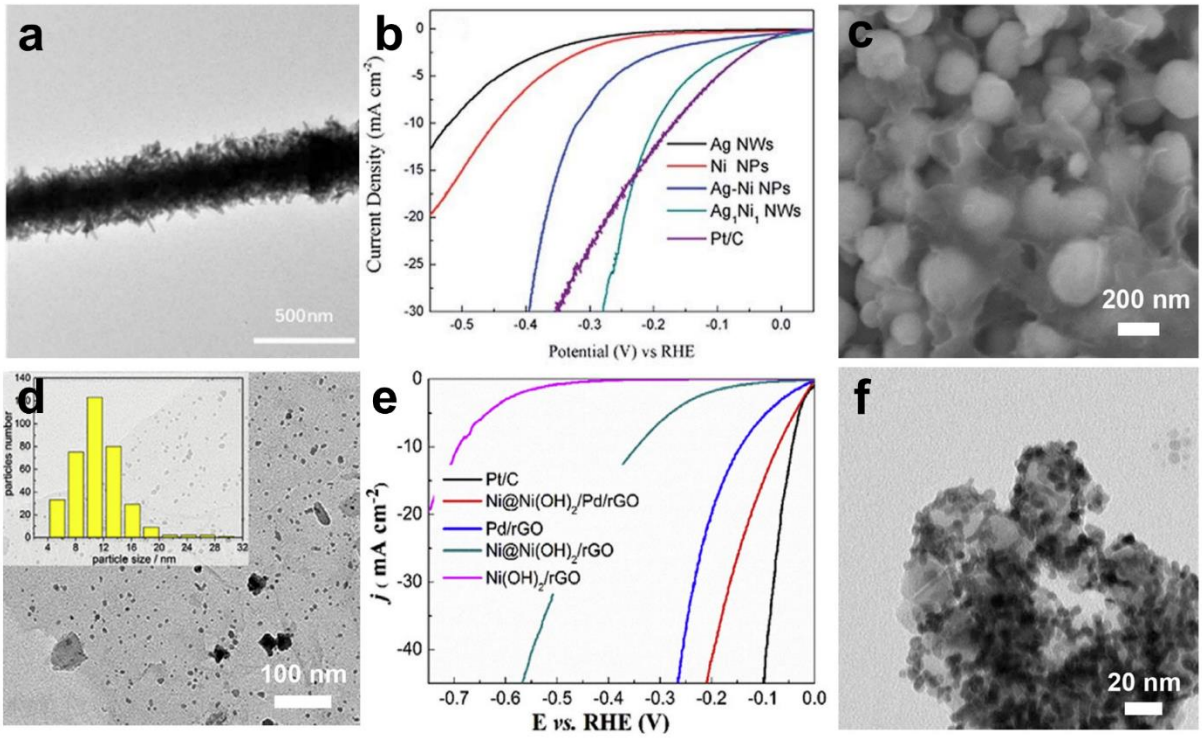

Figure 11. (a) TEM image of Ag-Ni nanowires with an atomic ratio of Ag to Ni of 1:1. (b) LSV curves of various catalysts as indicated, electrolyte: 0.1 M KOH, catalyst loading: 0.12 mg cm^{-2}, sweep rate: 10 mV s^{-1}. Reproduced with permission.[192] Copyright 2017, The Royal Society of Chemistry. (c) SEM image of $Ni@Ni(OH)_2$/RGO heterostructure without Pd seed. (d) TEM image $Ni@Ni(OH)_2$/Pd/RGO, the inset is the statistical particle size from 356 particles. (e) LSV curves of various catalysts as indicated, electrolyte: 1 M KOH, catalyst loading: 0.25 mg cm^{-2}, sweep rate: 5 mV s^{-1}. Reproduced with permission.[206] Copyright 2017, Elsevier Ltd. (f) TEM image of Pt/RTO heterostructure. Reproduced with permission.[194] Copyright 2017, permission conveyed through Copyright Clearance Center, Inc.

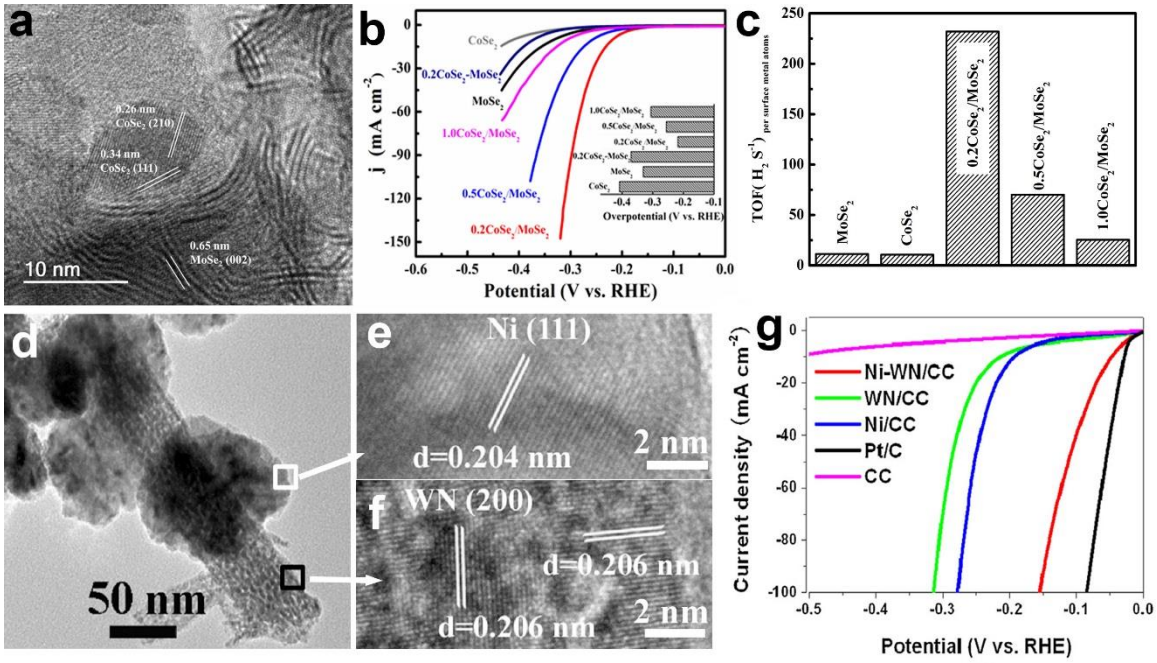

Figure 12. (a) TEM image of $0.2CoSe_2/MoSe_2$ heterostructures. (b) LSV curves of various catalysts as indicated, the inset is the overpotential at 10 mA cm^{-2}, electrolyte: 1 M KOH, catalyst loading: 0.2 mg cm^{-2}, sweep rate: 5 mV s^{-1}. (c) TOF at the overpotential of 300 mV. Reproduced with permission.[200] Copyright 2018, John Wiley and Sons (d) TEM image of Ni-WN. HRTEM of (e) Ni and (f) WN, corresponding to the white and black square in d. (g) LSV curves of various electrode as indicated, electrolyte: 1 M KOH, sweep rate: 5 mV s^{-1}, catalyst loading: 8.9, 4.5, 4.4 mg cm^{-2} for Ni-WN, WN, Ni, respectively. Reproduced with permission.[204] Copyright 2016, Elsevier Ltd.

Table 1. Heterostructures for HER in acidic solutions

Catalyst	Morphology	Electrode	Overpotential @10 mA cm^{-2} (mV)	Tafel slope (mV dec^{-1})	Catalyst loading (mg cm^{-2})	Sweep rate (mV s^{-1})	Electrolyte	Reference
1.82 % Pt/NPC	Pt nanoparticles on a 3D N, P co-doped carbon network	GC	20	36	0.28	50	0.5 M H_2SO_4	149
5.2% Rh-MoS_2	Rh nanoparticles on MoS_2 nanosheets	GC	~50	24	0.31	5	0.5 M H_2SO_4	146
Ag_2S/Ag	Ag_2S/Ag nanowires	GC	199	10_2	1.06	20	0.5 M H_2SO_4	147
Ag_2S/CuS	Nanoporous Ag_2S/CuS composites	GC	~190	75	0.28	5	0.5 M H_2SO_4	207

Ag_2S/MoS_2	Ag_2S nanoparticle-decorated MoS_2 nanosheets	ITO	~200	42		5	0.5 M H_2SO_4	115
Co_3S_4/CoP	Porous Co_3S_4/CoP nanorods	GC	86	45	0.28	5	0.5 M H_2SO_4	129
$Co_9S_8/MoS_x/C$ C	3D flower-like MoS_x incorporated Co_9S_8 nanosheets supported on CC	CC	98	65		0.5	0.5 M H_2SO_4	114
Co-FeS_2/CNT	Cobalt-doped FeS_2 nanosheets grown on CNTs	GC	160	46	0.4	1	0.5 M H_2SO_4	55
CoNi@NC	CoNi nanoparticles encapsulated in few-layered	GC	142	105	1.6	2	0.1 M H_2SO_4	98

	graphene spheres							
CoP/MoS_2-CNT	CoP *in situ* grown on MoS_2 and CNT	GC	12	42		5	0.5 M H_2SO_4	131
CoP/NSGO	CoP nanorods *in situ* grown on N,S codoped-GO	GC	~150	5_2	0.4	10	0.5 M H_2SO_4	103
CoP/WS_2	CoP nanoparticles combined with WS_2 nanosheets	GC	150	86	0.29	5	0.5 M H_2SO_4	130
CoS_2/Co_3O_4	Core-shell Co_3O_4/CoS_2 nanoneedle arrays on CC	CC	~150	45		2	0.5 M H_2SO_4	208
$CoS_2/CoSe_2$	CoS_2 nanoparticles dotted on $CoSe_2$/DETA nanobelts	GC	80	34	0.28	5	0.5 M H_2SO_4	113

CoS_2/MoS_2/CNT	Hybridized CoS_2/MoS_2 grown on CNTs	GC	180	67	0.35	5	0.5 M H_2SO_4	118
CoS_2/MoS_2/RGO	Ternary CoS_2/MoS_2/RGO heterostructure with CoMoS phase	GC	160	56		5	0.5 M H_2SO_4	119
CoS_2/RGO-CNT	*In situ* grown CoS_2/RGO uniformly distributed in CNT networks	Freestanding	142	51		2	0.5 M H_2SO_4	106
Co_xS_y/WS_2/CC	Co_xS_y/WS_2 nanosheets supported on CC	CC	120	89		5	0.5 M H_2SO_4	209
$Cu_{2-x}S$/Ru	Cactus-like hollow $Cu_{2-x}S$/Ru Nanoplates	GC	82	48	0.23	2	0.5 M H_2SO_4	210

CuS/Au	Au nanoparticle grown on the surface of CuS	GC	179	75	2.55	50	0.5 M H_2SO_4	151
Fe_2P/C	Carbon-coated hollow mesoporous FeP microcubes	GC	115	56	0.72	5	0.5 M H_2SO_4	123
Fe_2P/RGO/Fe_2P	Fe_2P/RGO/Fe_2P sandwich-structure	Ti plate	101	55		2	0.5 M H_2SO_4	125
FeCo@NCNTs -NH	FeCo alloy encapsulated in N-doped CNT with increased N	GC	~280	70	0.28	2	0.1 M H_2SO_4	97
FeP/Carbon	Carbon-shell-protected FeP nanoparticles	GC	71	52			0.5 M H_2SO_4	35

FeP/graphene	FeP nanoparticles grown on graphene sheets	GC	123	50	0.28	5	0.5 M H_2SO_4	37
Mo_2C-Mo_2N/C NT	β-Mo_2C and γ-Mo_2N nanoparticles grown on CNTs	GC	96	37	0.4	2	1 M H_2SO_4	205
MoO_2/N-MoS_2	MoO_2 nanobelts hybridized with N-doped MoS_2 nanosheets	GC	~210	48	0.28	5	0.5 M H_2SO_4	63
MoO_2/WN/Mo_2N	MoO_2/WN/Mo_2N grown on N-doped graphene	GC	120	84	0.21		0.5 M H_2SO_4	211
MoO_3/MoS_2	Vertically oriented core-shell MoO_3-MoS_2	FTO	~250	~55		5	0.5 M H_2SO_4	135

	nanowires							
MoO_x/MoS_2	Aligned MoO_x/MoS_2 core-shell nanotubular *in situ* grown on Mo foils	Mo foil	259	63		5	0.5 M H_2SO_4	138
MoS_2/Au	Spontaneous gold nanoparticle decorated MoS_2	GC	~330	57		5	0.5 M H_2SO_4	152
MoS_2/C	Amorphous MoS_2 supported by carbon black	GC	122	39	0.28	5	0.5 M H_2SO_4	107
MoS_2/CNT	Low-crystalline MoS_2 nanosheet coated on CNT network	GC	~175	45	0.136	5	0.5 M H_2SO_4	92

$MoS_2/CoS_2/CC$	MoS_2 nanosheet-coated CoS_2 nanowire arrays on CC	CC	87	73		5	0.5 M H_2SO_4	120
$MoS_2/CoSe_2$	Quasi-amorphous MoS_2-coated $CoSe_2$	GC	68	36	0.28	2	0.5 M H_2SO_4	49
$MoS_2/Fe3O_4$	Shell-core MoS_2 nanosheets/Fe_3O_4 sphere heterostructure	GC	~210	52	0.14	5	0.5 M H_2SO_4	136
MoS_2/MGF	*In situ* formation of MoS_2 nanoparticles on mesoporous graphene foams	GC	~100	42	0.21	2	0.5 M H_2SO_4	75
MoS_2/MoO_2	3D heterostructures of MoS_2	CC	~200	35.6		5	0.5 M	52

	nanosheets on conducting MoO_2						H_2SO_4	
MoS_2/MoO_2	MoS_2/MoO_2 core-shell structure	GC	210	129	0.28	5	0.5 M H_2SO_4	137
MoS_2/MoO_2	MoS_2 nanosheets supported by porous metallic MoO_2	GC	240	76	0.22	5	0.5 M H_2SO_4	53
MoS_2/N-doped CNT	Amorphous MoS_2 layer bound at vertical N-doped carbon nanotube (NCNT) forest surface	GC	110	40	0.102	5	0.5 M H_2SO_4	104
MoS_2/RGO	MoS_2 Nanoparticles grown on Graphene	GC	~150	41	0.28	5	0.5 M H_2SO_4	74

MoS_2/RGO	Space-confined grown MoS_2 nanosheets on RGO	GC	~160	41	0.2	5	0.5 M H_2SO_4	212
$MoSe_2$/$CoSe_2$	Nanosheet-assembled hierarchical $MoSe_2$/$CoSe_2$ microcages	GC	~200	73	0.28	2	0.5 M H_2SO_4	116
$MoSe_2$/NiSe	Epitaxial $MoSe_2$/NiSe vertical heterostructures	GC	210	56	0.285	5	0.5 M H_2SO_4	58
$MoSe_2$/RGO	$MoSe_2$ sheets grown on RGO	GC	115	69	0.16	10	0.5 M H_2SO_4	99
Ni_2P/CoP	Ni_2P nanosheets/CoP nanowires on CC	CC	55	48		2	0.5 M H_2SO_4	127
Ni_2P/Graphene/	Ni_2P nanosheets on 3D	NF	75	51		5	0.5 M	96

NF	graphene/NF						H_2SO_4	
Ni_2P/Mo_2C/M WCNT	Ni_2P/Mo_2C hybridized with MWCNT	GC	154	83	0.2	5	0.5 M H_2SO_4	132
Ni_2P/MoS_2	Ni_2P nanoparticles on MoS_2 nanoflowers	GC	~200	76		10	0.5 M H_2SO_4	128
Ni_2P-Ni_5P_4-NS	3D self-supported biphasic Ni_5P_4-Ni_2P nanosheet array	NF	120	79		10	0.5 M H_2SO_4	126
NiCo/graphene	NiCo alloy encapsulated by graphene sheets	GC	224	104	0.32		0.5 M H_2SO_4	98
PANI/CoP HNWs-CFs	Polyaniline (PANI) nanodots decorated CoP hybrid nanowires	CF	57	34.5	0.8		0.5 M H_2SO_4	134

Pt/DNA	Pt nanoparticles anchored on self-assemblies of DNA molecules	GC	30	26	15 μg Pt cm^{-2}	2	0.5 M H_2SO_4	145
Pt/MoS_2	Epitaxial Pt/MoS_2 heterostructures	GC	50	40		2	0.5 M H_2SO_4	148
Pt/MoS_2/CC	Trace-Pt-decorated MoS_2 nanosheets supported on CC	CC	50(@50 mA cm^{-2})	49		2	0.5 M H_2SO_4	153
P-WN/RGO	P-modified WN/RGO	GC	85	54	0.34	5	0.5 M H_2SO_4	43
RGO/WS_2	Vertical-oriented WS_2 nanosheets decorated by ultrathin RGO	W foil	229	73		2	0.5 M H_2SO_4	102

Rh/Si	Rh nanoparticles grown on Si nanowires	GC	180 (@100 mA cm^{-2})	24	0.193		0.5 M H_2SO_4	213
W_2C/MWCNT	Ultrasmall phase-pure W_2C nanoparticles	GC	123	45	0.56	10	0.5 M H_2SO_4	105
WS_2/RGO	2D WS_2 nanosheets on RGO	GC	270	58	0.4	5	0.5 M H_2SO_4	100
W_xC@WS_2	Ravenala leaf-like W_xC on WS_2 nanotubes	GC	146	61	0.3	5	0.5 M H_2SO_4	59
ZnSe/$MoSe_2$	Arrays of ZnSe/$MoSe_2$ nanotubes on FTO	FTO	200	73		5	0.5 M H_2SO_4	117

Note: CC: carbon cloth, CF: Carbon fiber, FTO: fluorine-doped tin oxide, GC: glassy carbon electrode, ITO: indium tin oxide, NF: nickel foam

Table 2. Heterostructures for HER in alkaline solutions

Catalyst	Description	Electrode	Overpotential @10 mA cm^{-2} (mV)	Tafel slope (mV dec^{-1})	Catalyst loading (mg cm^{-2})	Sweep rate (mV s^{-1})	Electrolyte	Reference
1T-MoS_2/$Ni_{2+\delta}O_{\delta}(OH)_{2-\delta}$	Nickel hydr(oxy)oxide nanoparticles on 1T MoS_2 nanosheets	CFP	72	77	0.4 based on MoS_2	5	1 M KOH	170
Ag-Ni	Core/shell Ag/Ni nanowires	GC	197	84	0.12	10	0.1 M KOH	192
CeO_2/Cu_3P/NF	CeO_2/Cu_3P nanoarray supported on NF	NF	148(@20 mA cm^{-2})	132		5	1 M KOH	183

Co/Co_3O_4/NF	3D Crystalline/amorphous Co/Co_3O_4 core/shell nanosheets grown on NF	NF	90	44		2	1 M KOH	50
Co/CoP/NF	Crystalline/amorphous Co/CoP film electrodeposited on NF	NF	35	71		2	1 M NaOH	214
CoP-CeO_2	CoP/CeO_2 hybrid nanosheet film on TM	TM	45	43		2	1 M KOH	182
0.2$CoSe_2$/$MoSe_2$	Cubic phase $CoSe_2$ quantum dots decorated on $MoSe_2$ surface	GC	218	76	0.203	5	1 M KOH	200

MoS_2/NiCo-LDH	Vertical MoS_2 sheets hybridiized with NiCo-LDH	CFP	78	77		5	1 M KOH	169
MoS_2/NiS/MoO_3	MoS_2/NiS/MoO_3 nanowires on Ti foil	Ti foil	91	55		2	1 M KOH	184
$MoSe_2$/$Ni_{0.85}Se$	3D $MoSe_2$/$Ni_{0.85}Se$ nanowire network	NF	117	66	6.48	2	1 M KOH	45
$Ni(OH)_2$/CoS_2/CC	$Ni(OH)_2$/CoS_2 hybrid nanowire array on CC	CC	99(@20m A cm^{-2})	118		5	1 M KOH	60
$Ni(OH)_2$/CuS	Mesoporous nano-shelled amorphous $Ni(OH)_2$/crystalline CuS	GC	95	104	0.29	2	1 M KOH	171

	hollow spheres							
$Ni(OH)_2/Fe_2P/TM$	Amorphous $Ni(OH)_2$ decorated Fe_2P nanoarray supported by TM	TM	76	105	1.34	5	1 M KOH	173
$Ni(OH)_2/MoS_2/CC$	$Ni(OH)_2/MoS_2$ heterostructure supported by CC	CC	80	60		2	1 M KOH	168
$Ni(OH)_2/Ni_3N/TM$	$Ni(OH)_2/Ni_3N$ nanoarrays supported by TM	TM	72(@ 20mA cm^{-2})	86		5	1 M KOH	172
$Ni(OH)_2/PtO_2/TM$	$Ni(OH)_2/PtO_2$ hybrid nanosheet array	TM	31.4(@4 mA cm^{-2})	89		5	0.1 M KOH	174

	supported by TM							
Ni/CeO_2−CNT	Ni/CeO_2 nanointerfaces	CFP	90		0.8	5	1 M KOH	181
	coupled with CNTs							
Ni/graphene	Ni nanoparticles	NF	57	89		5	1 M NaOH	158
	supported on graphene							
	layers							
$Ni@Ni(OH)_2/Pd$	$Ni/Ni(OH)_2/Pd$	GC	76	70	0.25	5	1 M KOH	206
/RGO	heterostructure supported							
	on RGO sheets							
$NiCo_2S_4/Ni_3S_2/$	3D heteromorphic	NF	119	105.2		5	1 M KOH	215
NF	$NiCo_2S_4/Ni_3S_2$							
	nanosheetson NF							

NiO/Ni-CNT	Nanoscale NiO/Ni heterostructures formed on CNT sidewalls	GC	80	82	0.28	1	1 M KOH	180
Ni-P/MoSx	Electrodeposited hybrid Ni-P/MoS_x film	FTO	140	64		10	1 M KOH	202
Ni-WN/CC	Ni particles electrodeposited on WN/CC heterostructures	CC	47	71		5	1 M KOH	204
Pt/$Co(OH)_2$/CC	Ultrafine Pt nanoparticle-decorated $Co(OH)_2$ nanosheet arrays on CC	CC	32	70	6.9	5	1 M KOH	175

Pt/Ni	Pt-modified 3D Ni electrode		75 (@ 100 mA cm^{-2})	~120		1	1 M KOH	193
$Pt/Ni(OH)_2$	Ultrathin platinum nanowires grown on single-layered $Ni(OH)_2$	CC	~150			10	1 M KOH	176
PtO_2/Co(OH)F	Ultrafine PtO_2 nanoparticles coupled with Co(OH)F nanowire array	TM	160(@100 mA cm^{-2})	63	1.32	5	0.1 M KOH	185
RuCo/NC	RuCo nanoalloys encapsulated in nitrogen-doped graphene	GC	28	31	0.28	2	1 M KOH	161

RuO_2/NiO	RuO_2/NiO nanorods arrays on NF	NF	100 (@ 100 mA cm^{-2})	38.5		5	6 M NaOH	216
TiO2 NDs/Co nanotubes	Co nanotubes decorated with TiO_2 nanodots	CF	106	62	0.75	5	1 M KOH	186

Note: CC: carbon cloth, CF: Carbon fiber, CFP: carbon fiber paper, FTO: fluorine-doped tin oxide, GC: glassy carbon electrode, NF: nickel foam, TM: titanium mesh

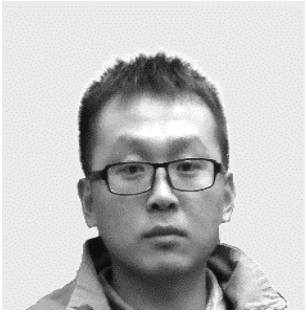

Guoqiang Zhao received his Bachelor degree from Harbin Engineering University in 2011 and Master degree from Institute of Metal Research, Chinese Academy of Sciences (IMR, CAS) in 2014. From Jul. 2014 to Dec. 2015, he worked as a Research Assistant in IMR, CAS. From Jan. 2016 to Jul. 2016, he worked as an Engineer in Amperex Technology Limited. Now he is a PhD student at the Institute for Superconducting & Electronic Materials at the University of Wollongong under the supervision of Dr. Wenping Sun and Prof. Shi Xue Dou. His research is focused on developing efficient catalysts for electrochemical water splitting.

Wenping Sun received his B.S. in 2008 and PhD in Materials Science in 2013 from University of Science and Technology of China (USTC). From September 2013 to May 2015, he worked as a Research Fellow at Nanyang Technological University, Singapore. In June 2015, he moved to Institute for Superconducting & Electronic Materials at the University of Wollongong. His research expertise includes batteries, electrocatalysis, and fuel cells, especially the design of novel materials and structures, and fundamental understanding of related electrochemical processes.

Recent research progress on heterostructured catalysts for electrochemical hydrogen evolution reaction (HER) are summarized in terms of materials design and synthesis, electrochemical performance, and the related mechanisms for performance enhancement. This review will not only provide new insights into designing low-cost and highly active HER catalysts, but also shed light on designing and synthesizing functional heterostructures towards a wide range of catalysis applications.

Electrocatalysis

Guoqiang Zhao, Kun Rui, Shi Xue Dou, Wenping Sun*

Heterostructures for Electrochemical Hydrogen Evolution Reaction: A Review

ToC figure